Key Points:
- Multiple cross faults ruptured to depth, into the oceanic mantle
- The highest moment release was on young faults, not the old fracture zone
- Sumatra GPS data help to constrain the strike of the unmapped faults

Correspondence to:
E. M. Hill,
ehill@ntu.edu.sg

The 2012 M_w 8.6 Wharton Basin sequence: A cascade of great earthquakes generated by near-orthogonal, young, oceanic mantle faults

Emma M. Hill[1], Han Yue[2], Sylvain Barbot[1], Thorne Lay[2], Paul Tapponnier[1], Iwan Hermawan[1], Judith Hubbard[1], Paramesh Banerjee[1], Lujia Feng[1], Danny Natawidjaja[3], and Kerry Sieh[1]

[1]Earth Observatory of Singapore, Nanyang Technological University, Singapore, Singapore, [2]Department of Earth and Planetary Sciences, University of California, Santa Cruz, California, USA, [3]LIPI Geoteknologi, Bandung, Indonesia

Abstract We improve constraints on the slip distribution and geometry of faults involved in the complex, multisegment, M_w 8.6 April 2012 Wharton Basin earthquake sequence by joint inversion of high-rate GPS data from the Sumatran GPS Array (SuGAr), teleseismic observations, source time functions from broadband surface waves, and far-field static GPS displacements. This sequence occurred under the Indian Ocean, ~400 km offshore Sumatra. The events are extraordinary for their unprecedented rupture of multiple cross faults, deep slip, large strike-slip magnitude, and potential role in the formation of a discrete plate boundary between the Indian and Australian plates. The SuGAr recorded static displacements of up to ~22 cm, along with time-varying arrivals from the complex faulting, which indicate that the majority of moment release was on young, WNW trending, right-lateral faults, counter to initial expectations that an old, lithospheric, NNE trending fracture zone played the primary role. The new faults are optimally oriented to accommodate the present-day stress field. Not only was the greatest moment released on the younger faults, but it was these that sustained very deep slip and high stress drop (>20 MPa). The rupture may have extended to depths of up to 60 km, suggesting that the oceanic lithosphere in the northern Wharton Basin may be cold and strong enough to sustain brittle failure at such depths. Alternatively, the rupture may have occurred with an alternative weakening mechanism, such as thermal runaway.

1. Introduction

The 11 April 2012 M_w 8.6 Wharton Basin earthquake sequence was both the largest strike-slip and largest intraplate earthquake sequence that has been instrumentally recorded. The events initiated ~400 km to the SW of northern Sumatra, Indonesia, on the oceanic side of the Sunda megathrust, within the Wharton Basin and just west of the Investigator Fracture Zone (Figure 1). The main shock sequence was followed 2 hours later by another great earthquake, of M_w 8.2, which initiated ~180 km to the south.

The point source centroid moment tensor (CMT) for the main shock was strike slip, with nodal planes striking at ~20° and 289° [http://www.globalcmt.org/CMTsearch.html]. Initially, it was assumed that the event must have ruptured one of the large, NNE trending left-lateral fracture zones that are prominent features of the Wharton Basin seafloor (Figure 2). These are old, deep, structural boundaries left over from the Eocene-aged Wharton spreading center [*Jacob et al.*, 2014], and geophysical investigations have found evidence for their active deformation [*Bull and Scrutton*, 1990; *Petroy and Wiens*, 1989; *DePlus et al.*, 1998; *Robinson et al.*, 2001; *Abercrombie et al.*, 2003; *Singh et al.*, 2011], suggesting they have been reactivated. However, a number of published seismological results for the 2012 event—including backprojection [*Meng et al.*, 2012; *Yue et al.*, 2012; *Ishii et al.*, 2013], W phase inversion [*Duputel et al.*, 2012], finite fault models from seismic data [*Yue et al.*, 2012; *Wei et al.*, 2013], and aftershock locations (Figure 2)—have indicated great complexity in the rupture pattern, with a cascading failure of multiple faults and, surprisingly, significant slip occurring on WNW trending, right-lateral faults that run approximately orthogonal to the NNE striking fracture zones. These WNW trending faults are likely to be much younger [e.g., *Carton et al.*, 2014]. Whether the WNW trending faults carried the majority of slip has been debated, with some studies [e.g., *Duputel et al.*, 2012; *Yue et al.*, 2012; *Ishii et al.*, 2013] preferring those faults, while others [e.g., *Satriano et al.*, 2012; *Wei et al.*, 2013] infer that the NNE trending structures had the greater slip.
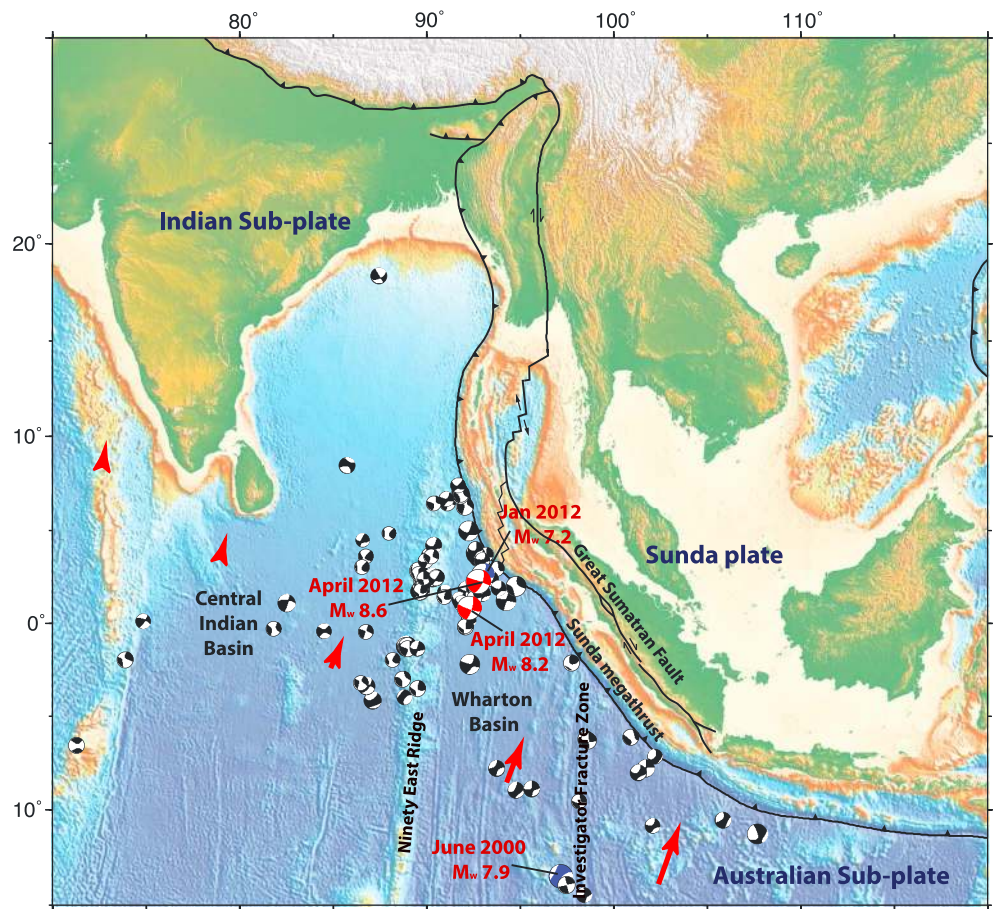
Figure 1. Location of the 11 April 2012 M_w 8.6 Indian Ocean earthquake with reference to its regional tectonic setting. Vectors are representative and simply indicate the expected difference in plate rates across the Indian-Australian Plates. Fault traces (solid black lines) were from *Bird* [2003] but we updated some by hand to reflect more accurate locations and added some extra lines to represent faults that were not included in the original data set. Focal mechanisms indicate the location of this event sequence, and its foreshock and aftershock. We plotted all > M4 strike-slip Global CMT solutions [*Ekström et al.*, 2012] from 1976 to December 2012 that occurred west of the Sunda Trench. The topography and bathymetry are from ETOPO1 [*Amante and Eakins*, 2009].

The seismological results also suggest that the ruptures likely extended from the surface, through the very thin (~4 km) [*Singh et al.*, 2011] oceanic crust, and significantly into the uppermost mantle, with a centroid depth of ~30 km [*Duputel et al.*, 2012]. It is difficult to tell from seismic data alone the maximum depth to which slip extended, but geophysical surveys do, indeed, show evidence that the NNE trending structures extend through the Moho [*Bull and Scrutton*, 1990; *Delescluse and Chamot-Rooke*, 2008; *Singh et al.*, 2011; *Carton et al.*, 2014]. Published finite-fault inversions based on teleseismic data estimate significant amounts of slip locally extending as deep as 50–60 km [*Yue et al.*, 2012; *Wei et al.*, 2013].

The location of the April 2012 events, especially with potentially deep rupture of the younger, unexpected faults, is intriguing. Scientists have long been puzzled by the nature and location of the boundary between the Indian and Australian Plates within the Indian Ocean [*Stein and Okal*, 1978; *Wiens et al.*, 1985; *Petroy and Wiens*, 1989; *Royer and Gordon*, 1997; *DePlus et al.*, 1998; *Gordon*, 1998]. Because of the resistance provided by the collision of India with Eurasia far to the north, the Indian plate is moving northward ~1 cm/yr slower than the Australian plate, which is subject to slab pull forces along the Sunda megathrust to the east (Figure 1); this difference in velocity creates strain between the Indian and Australian Plates, which may have been moving together as a single plate prior to the closing of the Tethys Sea. The India-Eurasia collision results in N-S compression in the Central Indian Basin. In the Wharton Basin, it results in NW-SE compression, while slab pull forces along the Sunda megathrust result in NE-SW extension [*Cloetingh and Wortel*, 1986; *Delescluse et al.*, 2012; *Andrade and Rajendran*, 2014]. These forces manifest themselves as a diffuse zone
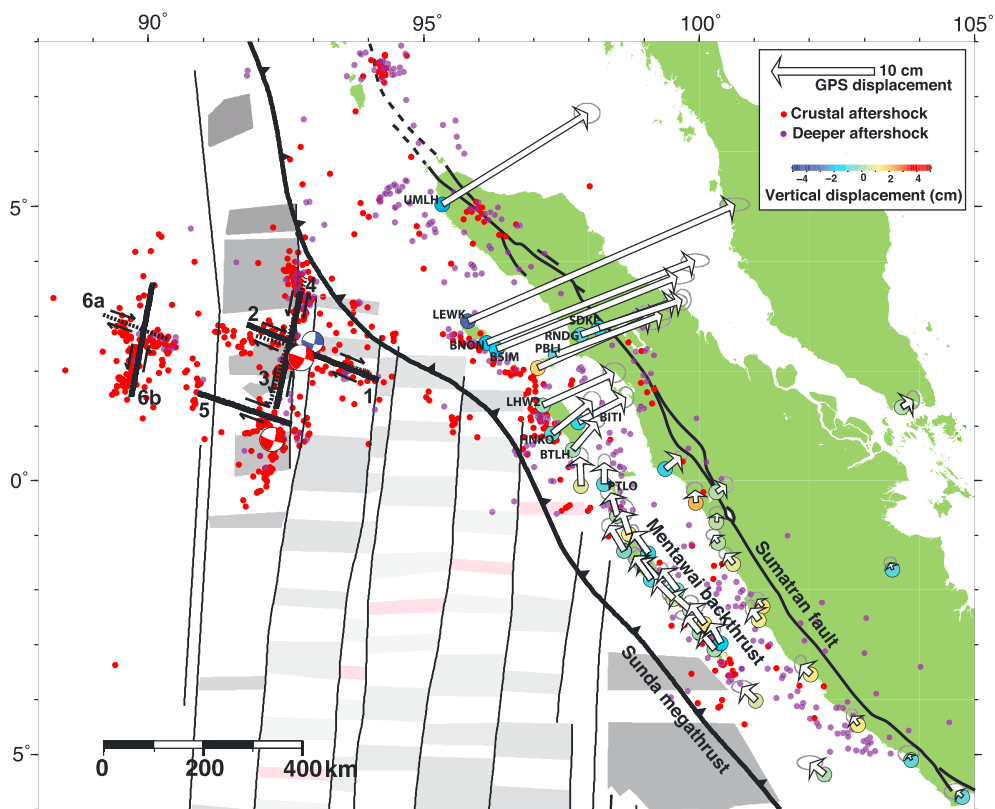
Figure 2. The April 2012 event ruptured several near-orthogonal faults. The solid black lines indicate our optimized geometry (as discussed in section 2). The dotted black lines indicate the geometry of *Yue et al.* [2012]. Faults 6a and 6b are two alternative geometries for the westernmost fault. While both orientations may have ruptured, our results suggest that rupture of 6b produces a slightly better fit to the late arrivals in the hrGPS data. White vectors indicate static horizontal displacements from daily SuGAr solutions; these contain the effects of both the M_s 8.6 sequence and the M_s 8.2 aftershock. Colored circles at the GPS station locations indicate vertical GPS displacements from daily solutions. Error ellipses are 95% confidence and are scaled as used in the inversions. The vertical displacements have large uncertainties. Thin black lines are from Figure 2 of *Singh et al.* [2011] and represent fracture zones identified from altimetry data. Shaded gray areas represent different plate ages, from *Jacob et al.* [2014], from ~38 Ma in pink through to ~66 Ma in dark gray. Aftershocks are plotted through April 2014, with data from NEIC and the depth of the crust extracted from the LITHO1.0 model [*Pasyanos et al.*, 2014]. The focal mechanisms are as labeled in Figure 1.

of deformation spreading across these basins (Figure 1), with evidence for this including earthquake focal mechanisms [*Stein and Okal*, 1978; *Petroy and Wiens*, 1989; *Tinnon et al.*, 1995; *Andrade and Rajendran*, 2014], plate spreading rates from magnetic anomalies [*Singh et al.*, 2011; *Jacob et al.*, 2014], geophysical surveys [*Chamot-Rooke et al.*, 1993; *DePlus et al.*, 1998], basement undulations inferred from gravity data that suggest buckling of the lithosphere in response to the compressive stresses [*McAdoo and Sandwell*, 1985; *DePlus*, 2001; *Subrahmanyam et al.*, 2008], stress modeling [*Cloetingh and Wortel*, 1986], and observations of relative plate motion [*Minster and Jordan*, 1978; *Royer and Gordon*, 1997]. The Ninety East Ridge (NER) serves as a relatively abrupt divide between differing deformation styles of the Central Indian Basin and the Wharton Basin (Figure 1), with a pattern of predominantly reverse faulting on E-W trending faults in the Central Indian Basin, and mostly strike-slip faulting in the Wharton Basin [*DePlus*, 2001; *Sager et al.*, 2013; *Andrade and Rajendran*, 2014].

It is possible that we are currently observing the slow transition from a diffuse deformation zone to a localized plate boundary between the Indian and Australian plates; the 2012 events may have played a role in this. This is particularly pertinent given the fact that some published results [e.g., *Wei et al.*, 2013] indicate fault planes that are not aligned with existing structures, suggesting the possible activation of newly formed faults.

The 2012 events were recorded by the Sumatran GPS Array (SuGAr). The SuGAr is a network of 60 continuous GPS stations situated along the Sumatra subduction zone (Figure 2), operated and maintained by the Earth

Observatory of Singapore (EOS) and the Indonesian Institute of Sciences (LIPI). The network observed NE static displacements of up to ~22 cm, on the island of Simeulue, with subsidence of up to ~4 cm. The significant distance of the main shock from land means that inversion of the static GPS displacements for distributed slip is poorly constrained. However, the GPS data are available at 1-second sampling, thus recording both seismic wave ground motions during the earthquake and static displacements. In this study, we combine near-field high-rate GPS (hrGPS) observations from the SuGAr with teleseismic data from the global network, source time functions extracted from broadband surface waves, and static GPS displacements from far-field SuGAr stations and a network in the Andaman-Nicobar islands, in a joint inversion for kinematic earthquake rupture. The hrGPS data for this event are unique to this study and improve the stability of inversion through self-consistent treatment of both the seismic waveforms and static displacements contained in their time series. For this event, the hrGPS data are recorded at regional distances, which improve sensitivity to rupture details while avoiding problems such as clipping and limited low-frequency resolution that are common for regional seismic recordings. We also incorporate geological and geophysical survey information, in the form of constraints on fault geometry, and information on rupture timing from published backprojection results.

This is not a simple modeling problem. We are combining a large number of different data sets, while also working with an inversion that contains a large number of estimated and unknown parameters (e.g., the event involved up to six different faults with poorly known geometries) and a relatively large distance from all available data networks. We therefore focus our efforts on determining, at the big-picture level, the extent to which we can answer a number of specific questions:

1. Do our data resolve whether the majority of moment release occurred on WNW trending faults, versus on the more prominent NNE trending structures evident in the seafloor fabric?
2. The main shock involved rupture of up to six fault segments in a single event. Although conjugate faulting has been observed in many other locations, it rarely involves so many fault segments and rarely in the same event. Can we provide any further constraints on the rupture propagation and number of faults that ruptured?
3. Can we provide better constraints on geometries and locations of these faults? Did the earthquake break new faults or reactivate old existing structures? And at what angle do the cross faults intersect? Previous studies [e.g., *Meng et al.*, 2012] have suggested that the faults intersect at a wide angle (~80°) compared to the expected angle of ~60° between conjugate shear faults (for a coefficient of friction of 0.6). If this wide angle is correct, is it the result of the existing structures?
4. How deep was the slip for this event? To what extent did it rupture the oceanic mantle? From a technical perspective, what depth resolution is achieved when we combine our various data sets?
5. The size (great strike-slip earthquakes are very rare) and location (away from major plate boundaries) of this sequence present some challenges to previous notions about strike-slip earthquakes. Was the large magnitude the result of high stress drop, the large number of faults involved, and/or the fact that it ruptured mantle material, which has much higher mechanical strength than the crust? How different, in terms of the rupture physics, was this event compared to other great earthquakes occurring in more "conventional" locations?

2. Data

We perform a joint inversion using near-field hrGPS data from the SuGAr network, far-field GPS static displacements, and teleseismic and broadband surface wave data from global networks. We also place constraints on our inversion from geometry and timing from geological/geophysical information and backprojection results, respectively. We here describe these data sets in more detail.

2.1. Near-Field, High-Rate GPS Time Series

We processed hrGPS data from the SuGAr network using Jet Propulsion Laboratory's (JPL) GPS Inferred Positioning System-Orbit Analysis Simulation Software (GIPSY-OASIS) II software in kinematic, Precise Point Positioning (PPP) mode [*Zumberge et al.*, 1997]. The kinematic processing scheme included estimation of time-varying station positions and tropospheric delays as stochastic random-walk processes, as well as resolution of carrier phase ambiguities [*Blewitt*, 1989; *Bertiger et al.*, 2010]. We tested a range of values for the random-walk variance to ensure that site position estimates were not biased by too loose or too tight constraints [*Elosegui et al.*, 1996]. For the PPP approach, the satellite orbits and clocks were held fixed to precise values from JPL, so the station positions could be estimated independently in the ITRF2008 reference frame and

are therefore not subject to errors inflicted by other stations in the network. A sidereal filter was tested but not applied, as this did not seem to result in cleaner time series for this particular solution. HrGPS time series data are provided in the supporting information.

Although the GPS were originally recorded at 1 s sampling, they were downsampled to an increment of 5 s for the inversion after being low pass filtered using a causal filter with a period of 25 s. The low pass filter was used because the corresponding Green's functions (which are computed for the preliminary reference Earth model (PREM)) do not accurately predict the shorter period signals. The Green's functions were treated with an identical filter (section 3). Unfiltered time series are shown in Figure S1 in the supporting information. Data for a 550 s time window were used in the inversion. Some stations were removed due to low signal-to-noise ratios (SNR), leaving a total of 21 included in the inversion. The vertical component, which is particularly noisy in kinematic solutions due to mismodeled atmospheric effects on the GPS signal propagation, was given only 20% weight compared to the horizontal time series (the relative weights between different data sets are described in section 3).

2.2. Far-Field, Static GPS Displacements

High-rate data from GPS stations in the SuGAr network far from the earthquake (>915 km) did not meet our SNR cutoff criteria. (The stations for which we used high-rate data are named in Figure 2; a map with names for all stations is given in Figure S2.) Examination of the far-field high-rate SuGAr time series confirms no discernible signal. However, daily GPS solutions have lower data noise. We were therefore able to obtain reliable static displacements, based on daily solutions, for an additional 21 far-field SuGAr stations. Offsets are plotted in Figure 2. These were estimated using 10 days of data before and after the earthquake, fit using an offset and a linear trend. In addition, static displacements from the Andaman-Nicobar continuous network, located ~500–1200 km north of the earthquake source, were published by *Yadev et al.* [2013], and we include these in our inversion. *Yadev et al.* [2013] also include some International Global Navigation Satellite Systems Service (IGS) stations, giving a total of 11 additional far-field stations from their data set. The maximum offset from the Andaman-Nicobar network is at Campbell Bay on Great Nicobar Island, ~41 mm toward the southeast. We use only horizontal displacements for the far-field stations (*Yadev et al.* [2013] did not include vertical displacements, and these are presumably very small).

Since they were obtained from daily solutions, the far-field offsets include the effects of both the main shock and the M_w 8.2 aftershock, as well as an early postseismic deformation. Offsets for the M_w 8.2 aftershock were observable in the hrGPS data for a few of the closest stations; at BNON and LEWK the horizontal offsets are on the order of ≤4 cm. We did not attempt to correct the daily solutions for these effects. However, the static GPS data were given low relative weight in the inversion (details of data weighting are given in the supporting information).

2.3. Broadband Teleseismic Data

We downloaded broadband teleseismic *P* and *SH* records from the Global Seismographic Network (GSN) from the Incorporated Research Institutions for Seismology (IRIS) data management center, for distances of 40 to 90°. To avoid an overabundance of data, the number of signals was then trimmed from hundreds to 63 using both an SNR cutoff and azimuth binning, as well as visual inspection for data quality. (Figure S3 shows the distribution of stations.) Instrument responses were deconvolved from the original data to give records of ground displacement. The data were also bandpass filtered with a pass band of 0.005 to 0.9 Hz. Teleseismic traces were aligned using manual picking of first arrivals and were cut to 200 s long records (following *P* or *SH* wave first arrival) for inversion, with some traces shortened to avoid *PP* phases. The sampling interval was reduced to 0.5 s.

2.4. Source Time Functions From Broadband Surface Waves

Broadband surface waves that have traveled along the great circle arc from source to station can be used to image variations in seismic moment release, once surface wave propagation effects are accounted for. In other words, the broadband surface wave recordings can be used to produce source time functions (STFs). For this study, we used global recordings of short-arc Rayleigh (R1) and Love (G1) waves to produce STFs. To remove propagation effects, Empirical Greens Functions (EGFs) were deconvolved from the main shock records. The EGFs were based on global R1 and G1 recordings for a foreshock event at a similar location (the 10 January 2012 M_w 7.2 event, with a source location at 2.45°N, 93.21°E, ~20 km NE of the April 2012 main shock location—Figure 2). The data are the same as those used in *Yue et al.* [2012], and more details

on the preprocessing and deconvolution are available in that paper. We used 21 R1 and 15 G1 STF traces in the inversion.

2.5. Fault Geometry

The initial fault geometry for the WNW trending right-lateral faults in our model (Faults 1, 2, and 5 in Figure 2) was based solely on the locations of aftershocks and published backprojection results [*Meng et al.*, 2012; *Yue et al.*, 2012; *Ishii et al.*, 2013], since there are no locally visible structures in the local bathymetry. Our original geometry had a strike of 286°, but we later adjusted this to 292° based on model fits to our data. The near-field GPS static displacements are particularly helpful for constraining the strike of the faults.

To determine the geometry of the NNE trending left-lateral faults, we examined published interpretations of seafloor bathymetry and magnetic anomalies [*Singh et al.*, 2011]. These mapped structures (Figure 2) have a strike of $\sim 7°$, and their location is difficult to reconcile with the aftershock and backprojection results. This suggests that the bathymetric and magnetic information may not be accurate enough; a proposed cruise will help with this (S. Singh, personal communication, 2014). We therefore place the NNE trending faults at the location determined by seismological results and set the strike of these faults to that of the Investigator Fracture Zone (IFZ), which can be more accurately defined to be $\sim 12°$ based on available high-resolution bathymetry. We here assume that the Eocene Wharton spreading Euler pole was far enough away that there was negligible difference between the IFZ strikes and that of the NNE trending fracture zone at the location of the 2012 main shock.

We also test models using the geometry of *Yue et al.* [2012]. Their faults were placed by examination solely of the backprojection and aftershock data. Their WNW trending faults have a strike of 286°, and the NNE faults strike at 16°. A comparison of the geometries is shown in Figure 2.

Our geometry differs considerably from the geometry of *Wei et al.* [2013], who used only three fault strands for their finite-fault inversion: a NNE trending fault striking 20°, a WNW fault striking 289°, and a single-fault striking 310° that runs approximately from the south end of our Fault 3 to the location of our Fault 6.

A strike of 16–20° is inconsistent with any mapped fracture zone strike on a large scale. This apparent strike could be accounted for by faulting on a set of en-echelon, right-stepping subsegments, each possibly with a transpressive component, along the fracture zone. This is not impossible and has been previously observed on ancient faults reactivated in a new stress field.

2.6. Timing Information From Backprojection Results

Kinematic inversion for so many fault segments involves many unknown parameters; in our case we estimate the moment of seven source time functions per patch, with six faults and a total of 120 patches in our full model. We therefore constrained the rupture initiation times in the inversion to results previously obtained using the backprojection technique [*Yue et al.*, 2012]. Specifically, fault segments were constrained to start rupturing at the times indicated in their text, and the rupture velocity was initially set to their estimate of 2.0 km/s. In initial tests we began the rupture at each fault segment at hypocenters determined in *Yue et al.* [2012] (projected to the nearest fault patch in our model), and a hypocenter depth of 22.5 km, which includes a water depth of 5 km (the U.S. Geological Survey-National Earthquake Information Center (NEIC) hypocenter depth is 20 km below Earth's surface, and 22.5 km is the nearest subfault midpoint depth in our fault mesh). However, we later made adjustments to the hypocenter depth as we explored the model space and modified the start time of Fault 2 (Figure 2) since our location is slightly different to that of *Yue et al.* [2012].

Published results [e.g., *Yue et al.*, 2012; *Ishii et al.*, 2013; *Wei et al.*, 2013] tell a reasonably consistent story that the rupture initiated on a WNW trending fault (approximately Faults 1 and 2 in Figure 2), then propagated to bilateral rupture of a NNE trending fault (Faults 3 and 4 in Figure 2). The rupture then jumped to an additional fault, or several, to the SW of these main faults (Faults 5 and 6 in Figure 2), accounting for the late arrivals seen in the high-rate and teleseismic data traces, and also for the early arrival of tsunami waves at stations located to the NW [*Ishii et al.*, 2013]. The start and stop times described in *Yue et al.* [2012] are reasonably consistent with values estimated in other studies [e.g., *Meng et al.*, 2012].

3. Modeling Strategy and Inversion

We discretized the faults into a number of rectangular patches (subfaults), with dimensions of ~15 km in the dip direction and ~30 km along strike. We also created model faults with single NNE and WNW trending
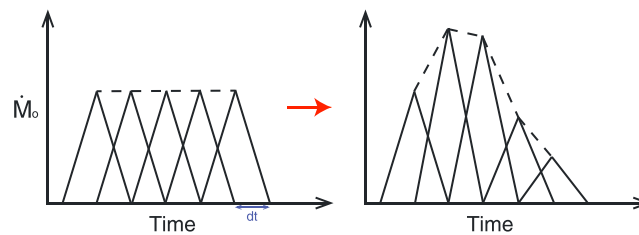
Figure 3. Example of how the source time function for each subfault is parameterized by a series of overlapping triangles. We start with a series of unit-moment triangles, then estimate the amplitudes of these in the inversion.

fault planes, for simple tests of which orientation bore the majority of moment release. These were, similarly, discretized into $\sim 20 \times 30$ km subfault patches. Unless otherwise stated, the faults were allowed to rupture to a depth of 60 km.

Our inversion technique uses a multi-time window approach [*Olsen and Apsel*, 1982; *Hartzell and Heaton*, 1983] and is similar to that described by *Yue and Lay* [2011] and *Yue et al.* [2013]. In this, a source time function (STF) is estimated for each subfault patch. The STF is parameterized by a series of overlapping triangles (Figure 3), and the estimated model parameters are the seismic moments of these triangles. For our inversion, we used seven STF triangles per subfault, with a half width (see Figure 3 for definition) of 3 s. This means that each subfault can rupture for a total of 24 s. (We did test many other combinations and concluded that these choices adequately capture the rupture; modifications do not significantly change our results.) We fixed fault timing, rupture velocity, rake, hypocenter location, and geometry for each inversion, based on prior information as described in section 2, but explored other values to either conclude that they did not affect our overall conclusions or have results as described below.

Green's functions used to model the hrGPS must include both static and dynamic ground displacements. These were obtained by summing all normal modes for the PREM velocity structure [*Dziewonski and Anderson*, 1981] up to 80 mHz and were provided as a mode set for a spherical, layered, anelastic Earth by Luis Rivera (Université de Strasbourg/Centre National de la Recherche Scientifique). The Green's functions are reliable for longer period (≥ 20 s) signals and epicentral distances ≥ 100 km [*Yue and Lay*, 2011; *Yue et al.*, 2013]. To facilitate dealing with a large number of subfaults and wide range of model geometries, we used a precalculated database. This database contains Green's functions for 10 km epicentral spacing and 1 km source-depth spacing, and we selected the nearest Green's function for each subfault/station configuration. Any errors due to differences between station distance and database distance are insignificant, given our frequency cutoff for the normal mode summation and the timing flexibility afforded by the multiple time window parameterization.

Prior to inversion, both hrGPS data and Green's functions were filtered using a low-pass filter with a period of 25 s. This reduces noise in the GPS data, mode truncation ringing in the Green's functions, and short-period signals that would be poorly predicted due to our use of a simple, 1-D, velocity structure. (Although the results are somewhat sensitive to the filter parameters, the basic results remain the same regardless of filter period.)

We used the same Green's function database for modeling the far-field static GPS displacements, but estimated the total static displacements from the Greens function time series and used these in the inversion. These have the advantage of being consistent with the high-rate functions and explicitly include spherical Earth effects.

To calculate the teleseismic Green's functions we used the reflectivity method procedure [*Kikuchi et al.*, 1993], which accounts for interaction in 1-D layered structures on both the source and receiver sides. For consistency with the other Green's functions we used the PREM velocity model for our calculations, but modified the water layer to a thickness of 5 km so as not to neglect the prolonged coda from water reverberations in this deepwater location. (We also tested models using a more local velocity model, obtaining similar results.) The Green's functions are band pass filtered using the same parameters as used for the data.

Green's functions for the surface wave STFs are a simple Gaussian curve that matches the averaging filter of the EGF deconvolution. Since both data and model estimates are STFs, the model relationship for these data is a simple scaling.
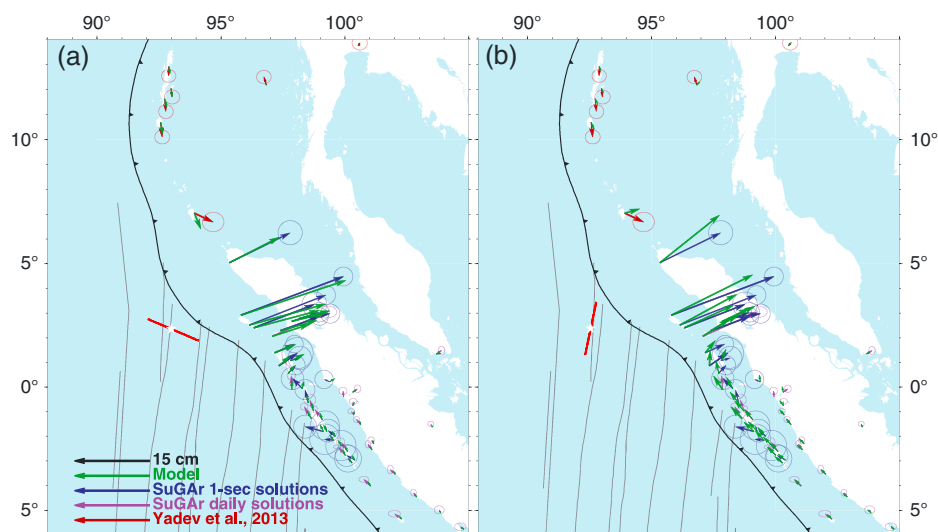
Figure 4. Comparison of predicted static displacements for (a) a single WNW trending, right-lateral and (b) a NNE trending, left-lateral fault. Data and model predictions are shown for both high-rate (blue) and daily (purple/red) GPS solutions. The red lines illustrate the surface projection of the faults, and the white stars the hypocenters used for the inversion. Error ellipses are 99% confidence and represent those used in the inversion, scaled as described in the supporting information. They do not show additional relative weighting between data sets as used in the inversions. Data-model residual vectors are shown in Figure S4. Although only the GPS static displacements are shown, all data sets (including hrGPS and teleseismic) were included in the inversions. We do not show slip distributions for these models, since we do not believe them to be accurately representative of this complex event. The red vectors (north of Sumatra) are from *Yadev et al.* [2013].

We normalized all data and Green's functions to achieve approximately unit variance for the data [*Harris and Segall*, 1987], and then individually weighted the data sets to achieve desired relative weights. For the final models, the hrGPS, teleseismic, and broadband surface wave data should receive approximately equal weight in the inversions. The static GPS displacements have little weight, given that they also contain the effects of the M_w 8.2 aftershock and postseismic deformation. A more detailed discussion of how the data were weighted is available in the supporting information.

We used spatial smoothing but not temporal smoothing. For most models we selected the smoothing weight using Akaike's Bayesian Information Criteria (ABIC) [*Akaike*, 1980], as outlined for earthquake slip inversions in *Sekiguchi et al.* [2000], although we explore alternative levels of smoothing in the supporting information. ABIC will select a smoothing weight based on the tradeoff between the norms of the data residuals and smoothed model parameters. The model fit to the teleseismic data is particularly sensitive to the level of smoothing.

After we estimated the model parameters (using a nonnegative least squares algorithm to constrain the rake [*Lawson and Hanson*, 1974]), we estimated predicted model time series for comparison with the data and converted the moment estimates to a slip distribution. In converting to slip, we used values for shear modulus at different subfault depths based on our layered Earth model (PREM). Since this is a kinematic model, we are able to visualize both cumulative slip and rupture propagation over time, although the rupture propagation is highly constrained by our a priori inputs on fault timing and rupture velocity.

We use estimates of "normalized, reduced chi-square" (χ_r^2: in our case this value is actually the weighted mean of the sum of the squares of the residuals, rather than a true chi-square value) to compare the models for different joint inversion setups. We are aware that this statistic is imperfect as a way to describe the fit of the models to the data. For example, certain features of the waveforms are more important to fit than others, but this is not captured in the statistic. However, we need some quantitative way to easily compare the results of changing the many user-defined parameters in the inversion.

4. Results

Although we combine several high-rate data sets, the large number of faults involved and distance from land means that inversion for the slip distribution of this earthquake is a poorly posed problem, and there are many
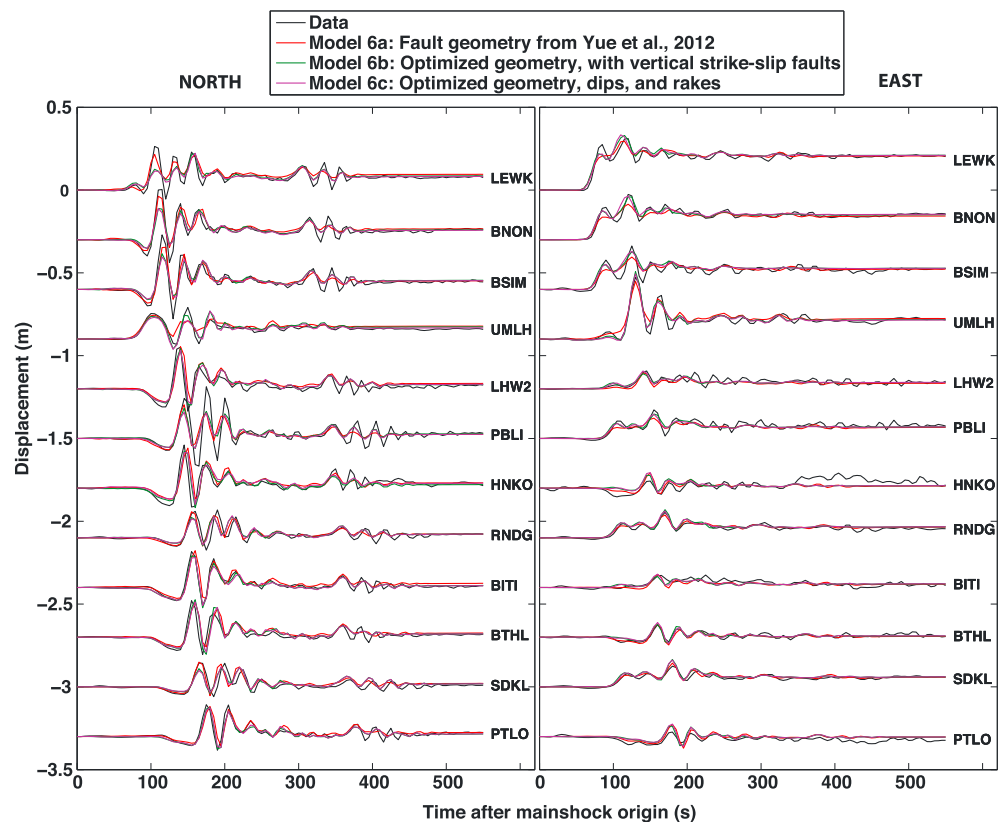
Figure 5. hrGPS time series for data and various models, for the closest GPS stations (additional stations are shown in Figure S5). The data are shown in black. Stations are ordered from closest to furthest from the main shock hypocenter, and station locations are given in Figure 2. Models are numbered (through the paper) according to the figure number for their slip distribution (Figure 6). Red lines indicate model predictions based on the fault geometry, rakes, and dips of *Yue et al.* [2012]. Green lines are for our optimized fault strikes, but with vertical, pure strike-slip faulting. Purple lines indicate predictions for a model that uses our optimized strikes, rakes, and dips. The data and Green's functions were low pass filtered prior to inversion (original time series are shown in Figure S1).

tradeoffs. Many parameters influence the results, including the fault geometry, the specified rupture velocity, the fault start times, the station distribution, uncertainties in Green's functions (e.g., from the seismic velocity model), the width and number of STF triangles used to parameterize the STF, the regularization technique and smoothing weight, and the relative weights given to different data sets. With these caveats, it is not possible to place reliable constraints on parameters such as the peak slip. However, we have explored the many controlling parameters in detail, and here discuss the results with a goal of identifying the key conclusions that remain robust and reliable. We include a discussion of model resolution in the supporting information.

4.1. Fault Geometry and Slip Distributions

As a first cut at assessing the relative amounts of slip on the WNW versus NNE trending fault structures, we performed single-fault inversions. The traces of these faults are shown in Figure 4. We chose the strike of the WNW trending fault to align with backprojection and aftershock data, and the strike of the NNE trending fault to align with the azimuth of the CMT solution, but later tested many other strikes with similar conclusions. Similarly, we initially set the faults to be vertical, with pure left-lateral and right-lateral strikes for the NNE and WNW trending planes, respectively, but later explored alternative rakes and dips with no changes to the overall conclusions.

When all data sets are included in these single-fault inversions, all have postfit residuals that are smaller for the WNW trending fault solution. The χ_r^2 misfit statistics for the hrGPS time series, static displacements from the hrGPS data, and teleseismic waveforms are 1.4, 2.0, and 1.4, respectively, for joint inversion of all data for the WNW model, compared to 2.2, 5.1, and 2.4 for the NNE trending fault model. The GPS static displacements are particularly sensitive to fault strike; note the significant increase in the misfit for the GPS
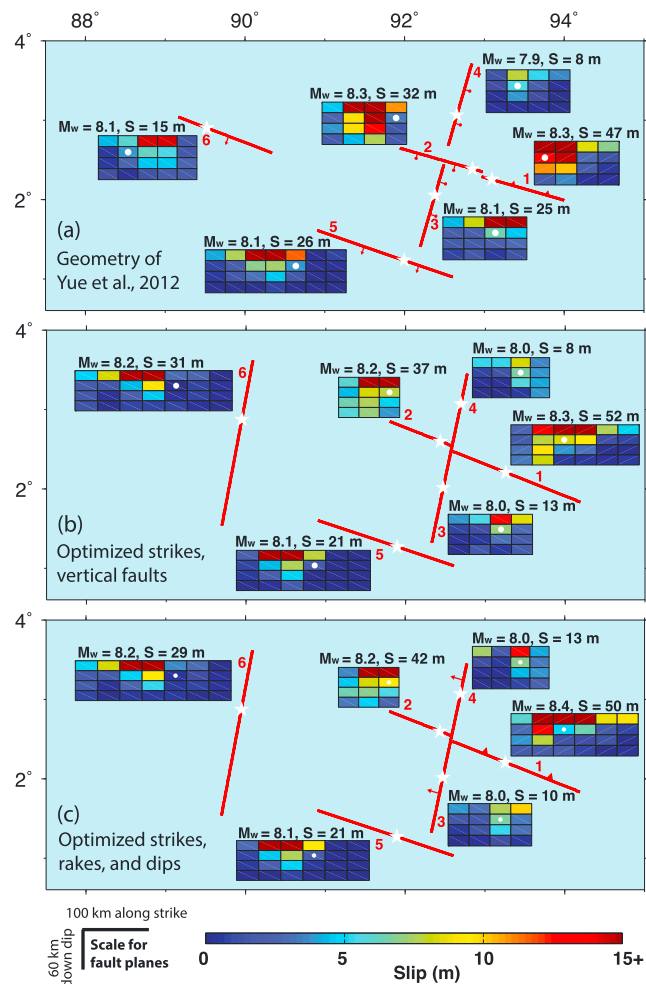
Figure 6. Slip distributions for models that use (a) the fault geometry of *Yue et al.* [2012], (b) our optimized strikes, with vertical faults and pure strike-slip motion, and (c) our optimized strikes, rakes, and dips. Slip on the bottom row of patches was penalized for all three models. The figure combines the faults (red lines) in map view, with the fault planes plotted next to each fault in planar view. The fault plans all have a bottom depth of 60 km but are plotted as distance along dip (as indicated in scale). The white stars and white dots indicate the hypocenter locations used in the inversion. These were derived from backprojection studies. Chi-square statistics for data and model predictions based on these models are shown in Figure 10. The color bar is saturated at 15 m slip, but maximum slip and moment magnitude are given above each fault plane. Figure S6 shows the same results plotted with a color bar saturated at 30 m.

static displacements, as illustrated in Figure 4. If the teleseismic data are inverted by themselves, either fault plane works fine, with similar χ_r^2 values. However, if the hrGPS data are inverted by themselves, the preference for a WNW oriented plane remains pronounced.

The model for a single, WNW trending structure fits the data surprisingly well, given the known complexity of the rupture. However, the time series predictions for the hrGPS data are flat at the times of the late arrivals seen in the data (after ~300 s in Figure 5). Faults further to the west are required to fit these waveforms.

Inversions produced using more complex geometries (as described in section 2.5) also place the majority of slip on the WNW trending faults (Figure 6). The modeled rupture on the WNW trending faults is deep, with patches of slip of 10–15 m as deep as 45 km and 5–10 m slip even deeper than this. The hrGPS (Figure 5), teleseismic (Figure 7), and EGF data (Figure 8) are generally well fit. The late arrivals in the hrGPS data are slightly better fit when the westernmost fault has left-lateral slip on a fault with a NNE orientation (i.e., aligned along the NER; Fault 6b in Figure 2), rather than right-lateral slip on a WNW trending fault (Fault 6a in Figure 2); this can be seen by comparing the traces for Model 1 and Model 3 at ≥300 s in Figure 5.
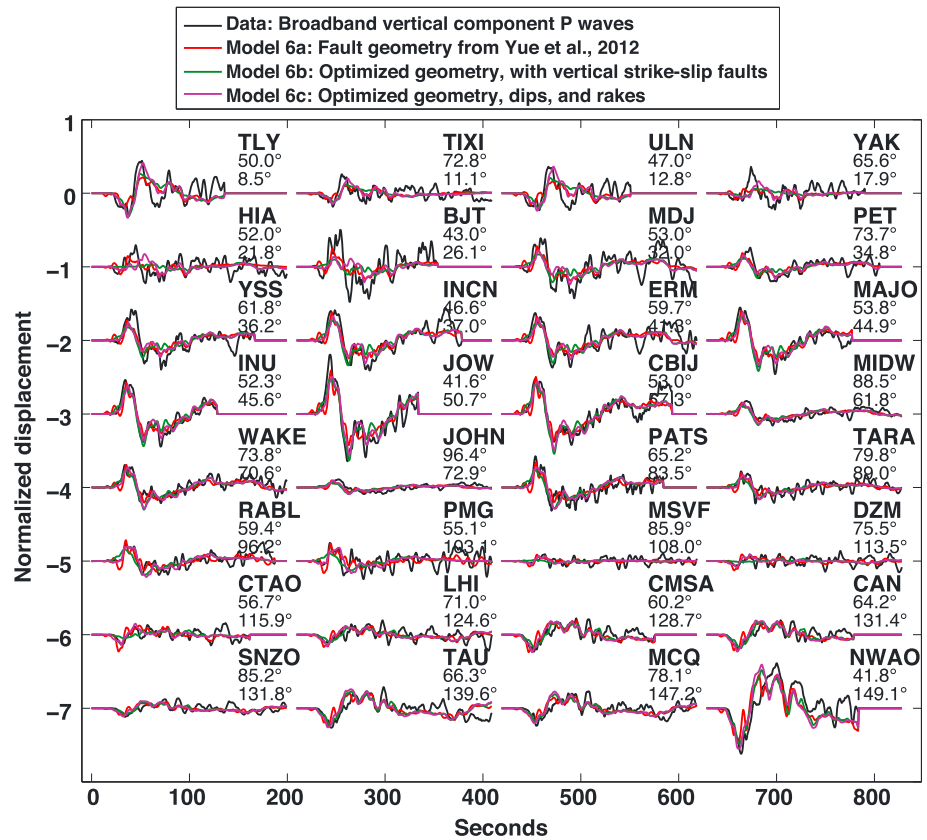
Figure 7. Teleseismic time series for data and various models, as described in the caption for Figure 5. Models are numbered according to the figure number for their slip distribution (Figure 6). The figure shows vertical component *P* wave data for only approximately one third of the stations. Additional stations and *SH* wave data are shown in Figures S6 and S7. The data and Green's functions were low pass filtered prior to inversion. The text shows the station name, the angular distance, and the azimuth from the source.

The static displacements (from the hrGPS data) are only fit well if the orientations of the WNW trending faults are optimized according to the nodal plane they require. The nodal plane is not optimal in the fault geometry of *Yue et al.* [2012], as demonstrated in Figure 9a by the fact that the model and data vectors are rotated relative to each other. Changing geometrical parameters such as rake and dip does not solve the problem of a misaligned nodal plane. We therefore ran a large collection of model tests aimed at optimizing the strike and location of the various faults in order to better fit the static displacements. The new geometry, as shown in Figure 2, has strikes for Faults 1 and 2 of 292°, compared with 286° for the model of *Yue et al.* [2012]. Since there is much less slip on the NNE trending faults, their strike did not significantly impact the displacements, so we left that at the strike determined by bathymetric mapping. The considerable improvement to the fits for the static displacements, when using the optimized fault strikes, is illustrated in Figures 9b and 10. (Note that Tables S1–S3 contain a summary of geometric parameters (fault coordinates, strikes, dips, rakes, and chi-square fits) for all models illustrated in this paper. We number the models by the figure number for their slip distribution, for easy reference.)

We ran the optimization for fault strike using vertical fault planes with pure strike-slip motion. However, this results in a degradation of the fits to the teleseismic data (Figure 10, models 6a and 6b), compared to those from models based on the *Yue et al.* [2012] geometry. We therefore performed a simple grid search to optimize the rakes and dips. We tested faults that had dips of ±70° or 90°, and rakes of either pure strike slip or strike slip with 10° of thrust or normal motion. We tested only this limited set of geometries and rakes because these parameters are poorly constrained by the data, and many combinations are equally viable in terms of data fit. For similar reasons, we did not try to optimize the rakes and dips for Faults 5 and 6, since these are far from the observing networks. The different data sets prefer different rake and dip combinations, so for the "preferred" model (model 6c) we selected those that work best for the teleseismic data, given that these are the most
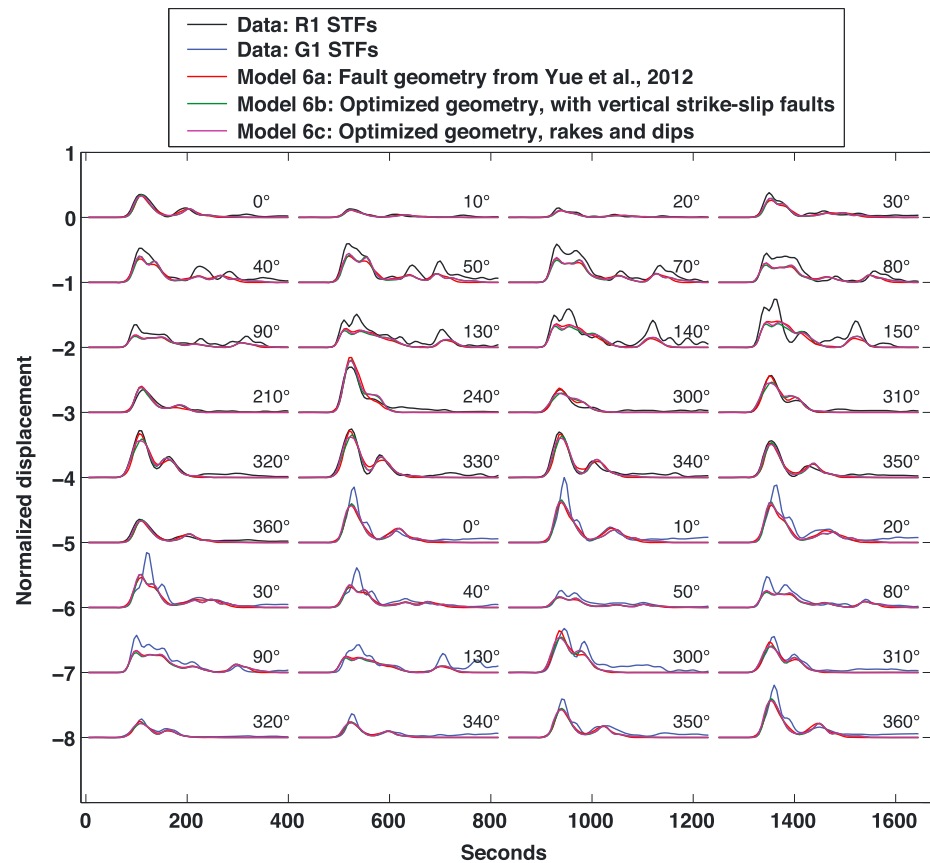
Figure 8. Source time functions from broadband surface waves for data and various models, as described in the caption for Figure 5. The STF data are stacked in 10° azimuthal bins and labeled with the central azimuth from the source for each stacking bin.

sensitive to these parameters. This model places Fault 1 as a north dipping thrust fault, keeps Fault 2 as vertical but gives it a rake of 170°, and puts Faults 3 and 4 as pure left-lateral motion on a fault that dips toward the west. Figures 6b and 6c compare slip distributions for a model with vertical faults and pure strike-slip motion, and a model using the optimized rakes and dips, respectively; optimizing the dips reduces the amount of very deep slip. Figures 7 and 10 illustrate that the fits to the teleseismic data are significantly improved with this simple optimization of rakes and dips, but we stress that many other combinations of rakes and dips are also viable.

Since the fault rakes and dips are not well constrained, we also show slip distributions for various alternatives in Figure 11, with associated model-data misfits shown in Figure 10. In Figure 11a, we selected a model with east dipping NNE trending faults, compared with west dipping as in our optimized model. We show this test because *Singh et al.* [2011] image the NNE trending faults to be east dipping further to the north of our rupture (but the dips may change along strike). In Figure 11b we show a model in which we use our optimized fault strikes, but the rakes and dips of *Yue et al.* [2012]. In Figure 11c we remove Fault 2, because there is ambiguity as to whether this fault shows up in backprojection results [*Meng et al.*, 2012; *Yue et al.*, 2012; *Ishii et al.*, 2013], although it is highlighted by aftershocks (Figure 2). In Figure 11d, Fault 1 is a south dipping normal fault. As shown in Figure 10, the only change that significantly affects the data fits is the removal of Fault 2.

Unfortunately, there is a remaining trade-off between fitting the first arrivals at the three closest GPS stations, and fitting the static GPS displacements. These first arrivals are better fit by the geometry from *Yue et al.* [2012] than with our new optimized geometry (Figure 5). Although we explored a large model space, we were unable to resolve these trade-offs. It is possible that they are the result of uncertainties in the velocity model.

The question of whether the rupture involved deep slip is an important one. We tackled this question by running a number of tests that encourage or penalize deep slip. The results are shown in Figures 12 and 10.
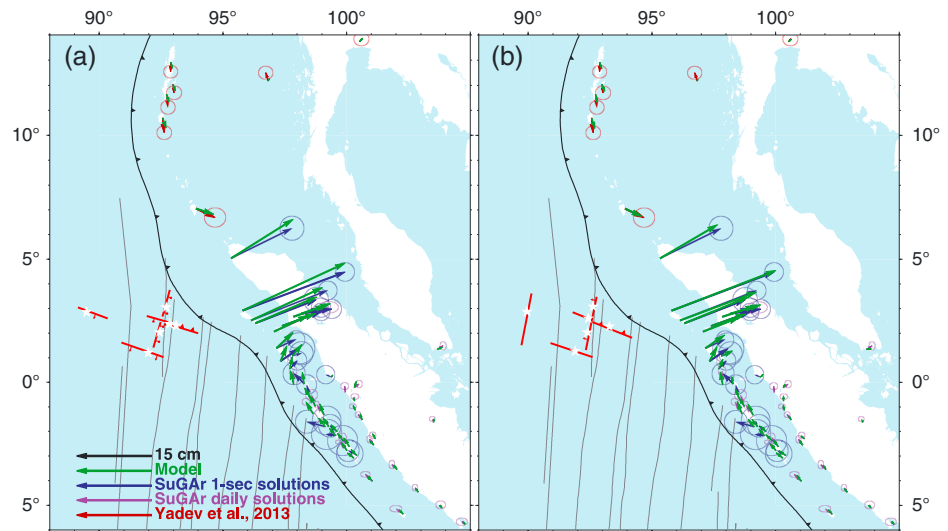
Figure 9. Comparison of predicted static displacements based on slip distributions for (a) the fault geometry of *Yue et al.* [2012] (Figures 2 and 6a) and (b) a geometry with optimized strikes, rakes, and dips (Figures 2 and 6c). Error ellipses are 99% confidence and represent those used in the inversion, scaled as described in the supporting information. They do not show additional relative weighting between data sets as used in the inversions. The red lines illustrate the surface projection of the faults, and the white stars the surface projection of the hypocenters used in the inversion. Data-model residual vectors are shown in Figure S9 and a figure that includes daily solution offsets for all stations in Figure S10.

In general, the data are fit as well by our "preferred" model (Figure 6c) as by any of the tests that allow deeper slip. The teleseismic data are the most sensitive to the depth of slip. They do not prefer more shallow or more deep hypocenters, that encourage shallower or deeper slip, but do slightly prefer a model in which slip is not penalized on the bottom row of fault patches (from 45-60 km depth). Our models do not rule out slip to depths of ≥80 km. We note also that the depth of slip is affected by the fault strike and geometry (Figure 6), which remains difficult to properly constrain.

As already stated, kinematic, finite-fault models always have a large number of tradeoffs between the large number of parameters that can be tweaked in the inversion, and this is particularly true for this event since
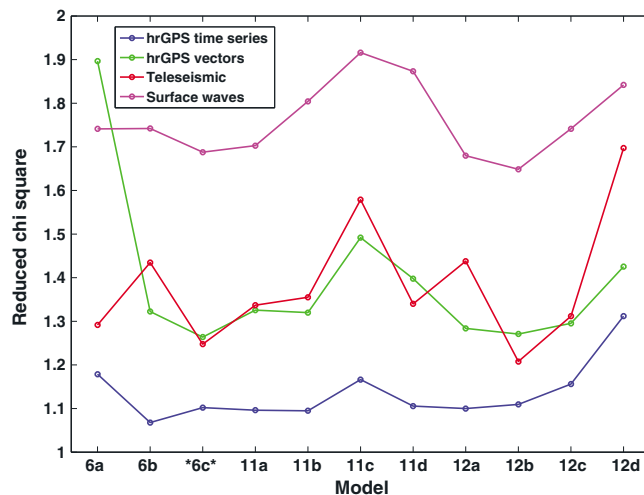

Figure 10. Differences in the reduced chi-square fit between data and model predictions. The models are numbered according to the figure number for their slip distribution, as indicated on the *x* axis. Tables S1 – S3 summarize the differences between the models. Our preferred model is 6c, as highlighted by asterisks. Note the significant improvement to fit when using the optimized fault strikes (from 6a to 6c). Note also the increased misfit when Fault 2 is removed (11c).
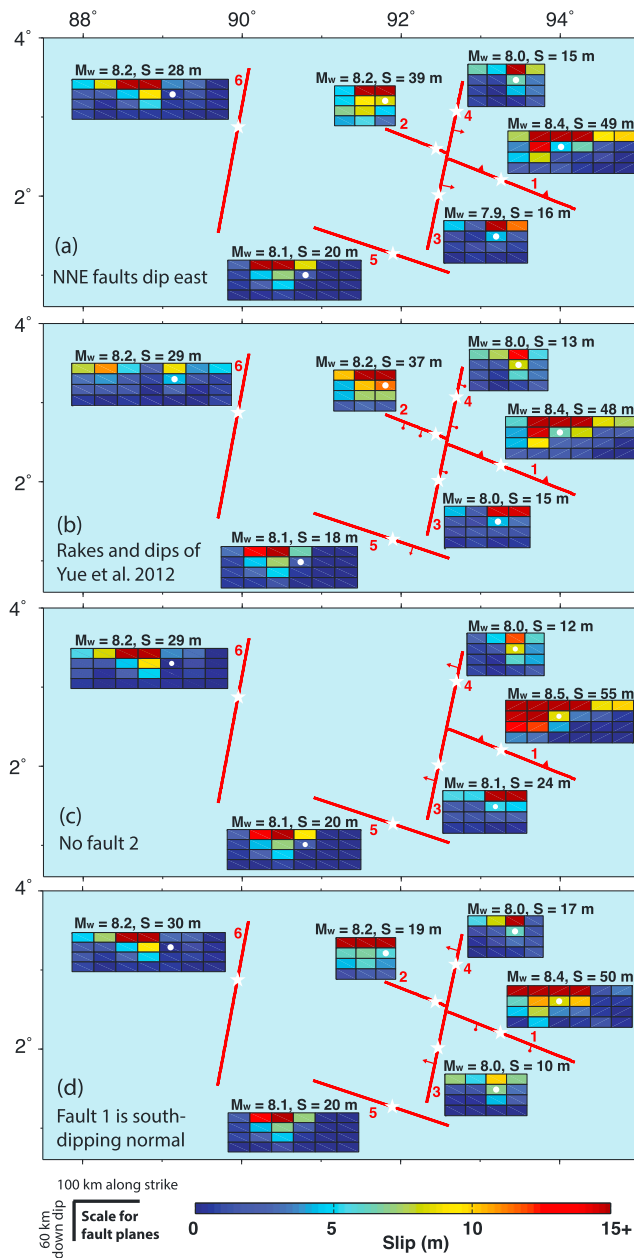
Figure 11. Slip distributions for models exploring a range of different fault dip and rake combinations. All strikes are fixed to the optimized values. (a) We switch the NNE trending faults to dip to the east instead of to the west. (b) We use our optimized geometry but the rakes and dips of *Yue et al.* [2012]. (c) We remove Fault 2. (d) Fault 1 is a south dipping normal (instead of thrust) fault. The data are not strongly sensitive to the variations in rake and dip. However, the removal of Fault 2 (Figure 11c) negatively impacts the model-data fits (Figure 10). The color bar is saturated at slip of 15 m. Slip on the bottom row of patches was penalized. The white stars and white dots indicate the hypocenter locations used in the inversion. Figure S11 shows the same results plotted with a color bar saturated at 30 m.

it involved such a large number of faults. For example, in this inversion technique the user predefines the hypocenter locations, fault start times, and rupture velocities. These all trade off each other; for example, a faster rupture velocity can accommodate misplacing of a hypocenter or an incorrect fault start time. It is therefore difficult to say anything definitive about parameters such as rupture velocity from our results. Similarly, the maximum fault slip and stress drop are highly susceptible to changes in the smoothing technique and weights used, so these parameters are not well constrained. We explore the effects of varying these types of parameters, as well as the effects of inverting the different data sets individually, in the supporting information. In all of these tests, the general features of the slip distribution remain similar. The most significant difference (beyond obvious effects such as changing slip amplitude with changes in spatial smoothing weight) is that moving the hypocenters can reduce the amount of deep slip.

4.2. Vertical Deformation Field

GPS and model estimates of vertical displacement are shown in Figure S13. Northern Sumatra experienced subsidence of ≤4 cm as a result of the earthquake. Although the vertical displacements were given very little weight in the inversion, the preferred model also predicts subsidence (albeit very small).

4.3. Stress Drop

We calculate the average stress drop $\Delta\tau$ for this event using the following methodology. We first compute the coseismic change in shear traction **t** at the center of each fault patch based on the finite slip distribution using the formulation of *Okada* [1992]. We use a uniform fault discretization, so the stress singularity at the termination of each fault patch has a minimal impact on this calculation. Nevertheless, we perform the stress change calculation using *dc3dm*, the numerical method of *Bradley* [2014], that produces results that are comparably accurate for both
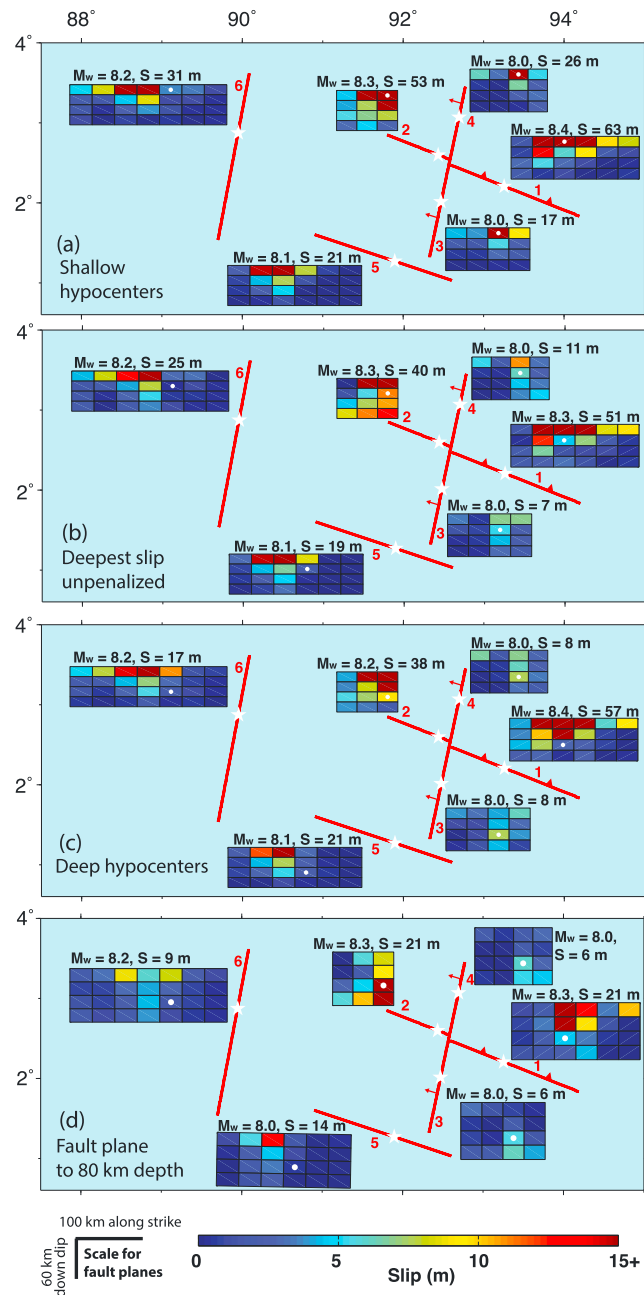
Figure 12. Slip distributions for a collection of models that investigate the effects of allowing or penalizing deep slip. The white stars and white dots indicate the hypocenter locations used in the inversion. (a) The hypocenters are adjusted to 7.5 km depth (compared to a depth of 22.5 km as used in other models). (b) The model is equivalent to that shown in Figure 6c, but slip on the bottom row is not penalized. (c) The hypocenters are adjusted to 37.5 km depth. (d) The faults are adjusted to have a bottom depth of 80 km and the hypocenters are deep. The color bar is saturated at slip of 15 m. Figure S12 shows the same results plotted with a color bar saturated at 30 m. The chi-square model to data fits for these slip distributions are shown in Figure 10.

uniform and nonuniform meshes. We then express the average stress drop using the formulation of *Noda et al.* [2013],

$$\Delta\tau = \frac{\int_{\partial\Omega} \mathbf{s} \cdot \mathbf{t}}{\int_{\partial\Omega} \sqrt{\mathbf{s} \cdot \mathbf{s}}} \tag{1}$$

where **s** represents coseismic slip and the integration is performed over the entire fault area $\partial\Omega$.
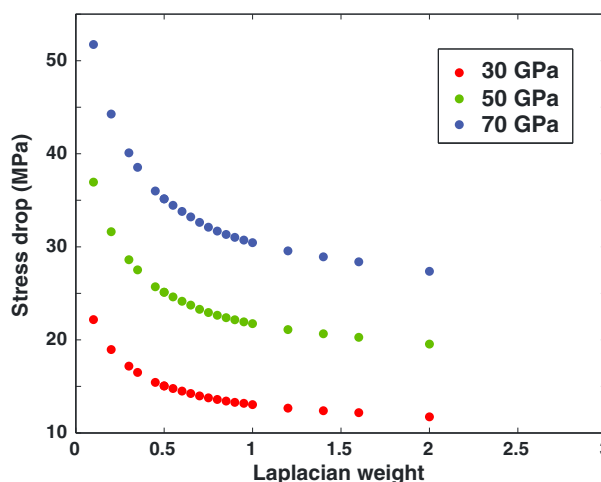
Figure 13. Changes in stress drop with respect to Laplacian smoothing weight (*x* axis) and shear modulus (color). The model shown in Figure 6c used a smoothing weight of 0.35, while the model shown in Figure S14a used a smoothing weight of 0.65.

This method of calculation helps to avoid inconsistencies in picking the rupture area for an inhomogenous slip distribution, which is a problem with the more simple analytical equation [*Kanamori and Anderson*, 1975]. In computing the stress drop distribution we fix the shear modulus to a constant (to facilitate comparisons), so the measure is a proxy for strain drop (also called potency). In Figure 13 we illustrate stress drop estimates for shear moduli of 30, 50, and 70 GPa. In our following discussions we use a shear modulus of 30 GPa.

We calculate a stress drop of 17 MPa for our preferred model (slip distribution shown in Figure 6c). However, stress drop is highly dependent on the regularization used. In Figure 13 we illustrate stress drop based on a range of different Laplacian smoothing weights. The stress drop for the model shown in Figure S14a, which has more spatial smoothing, is 14 MPa.

Perhaps more revealing are the relative differences in stress drops for individual fault segments. These are given, for the model shown in Figure 6c, in Table 1. The stress drop estimated for Faults 1 and 2 is considerably higher than for other fault segments.

4.4. Source Time Functions
Figure 14 shows estimated source time functions for each fault, for our preferred model. The rupture starts on Fault 1 with a large punch of initial energy, followed closely after by large peaks of energy release along Fault 2. Fault 3 begins rupturing just around the time that the large peak in moment release is ending on Fault 1, with bilateral rupture of Fault 4 beginning soon after. A final peak in moment release is displayed by Fault 6 (on the NER), from ~120 to 170 s.

Our preferred model has a total moment of 1.2×10^{22} N m, assuming a PREM rigidity model. This compares to values such as 9.2×10^{21} N m [*Duputel et al.*, 2012] and 1.3×10^{22} N m [*Wei et al.*, 2013].

5. Discussion

Our results show that the majority of moment for this event was released on WNW trending, right-lateral faults, with the primary two WNW trending faults (Faults 1 and 2 in Figure 2) bearing subevents of M_w ~8.4 and 8.2 (Figure 6). Although previously published results from teleseismic data were ambiguous as to the relative importance of the WNW trending faults, our GPS data (especially the static displacements) confirm that they played a key role. The GPS data also help us to place better constraints on the strike of these faults, estimated to be ~292°. We estimate that peak slip was on our Fault 1 (the closest WNW trending fault to the Sunda megathrust), and although we recognize that peak slip is an unstable parameter in these types of inversions, our results regularly place ≥50 m slip on this fault. The NNE trending, left-lateral fault (Faults 3 and 4 in Figure 2 (which lie along the same fault trace but were divided for timing purposes in the inversion)) was originally expected to be the main player in this event. This also accommodated significant slip, but with two smaller subevents of M_w ≤8.0 and peak slip estimated to be ≤20 m. The results further show that at least 5

Table 1. Stress Drop for Each Fault Segment, Based on the Preferred Model (Figure 6c)[a]

Fault Number	1	2	3	4	5	6
Stress drop (MPa)	25	19	4	5	9	11

[a] The mean stress drop for all faults is 17 MPa. These values were estimated using a constant shear modulus of 30 GPa.
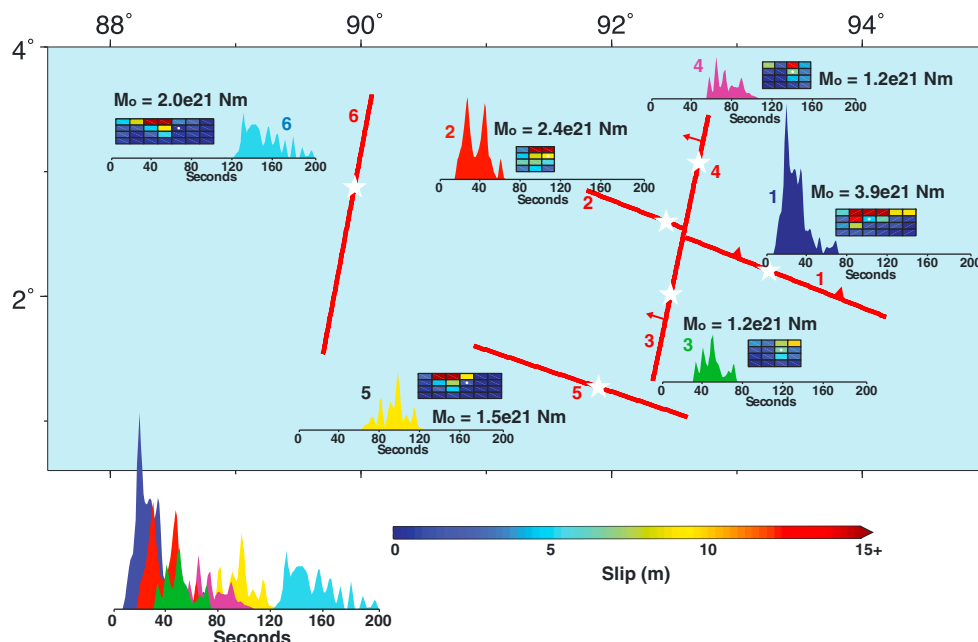
Figure 14. Source time functions for model 6c, which uses optimized strikes, dips, and rakes.

near-orthogonal faults ruptured over the course of this ~180 s event, with faults to the west of the main shock necessary for fitting late arrivals in the hrGPS time series. These western faults include a fault (or set of faults) along the NER (Fault 6 in Figure 2).

Our results consistently show slip to a depth of ≥45 km, particularly on the WNW trending faults. There are tradeoffs between fault dip/strike and the depth of rupture; previous results that did not have optimal fault locations may have overestimated the amount of deep slip because of this. There are also tradeoffs between depth and inaccuracies in the simplified velocity model we used. Regardless, our results confirm that the event ruptured deep into the lithosphere, through the thin crust and into the upper mantle. These results are consistent with the deep (~30 km) rupture centroid estimated by *Duputel et al.* [2012] for both the main shock and the M_w 8.2 aftershock.

There remains the question as to whether this event broke the seafloor. Based on the high levels of shallow slip, the answer seems likely to be yes. A planned cruise (S. Singh, personal communication, 2014) may answer this question more conclusively, as well as confirm the location and geometry of the faults.

In the following subsections we discuss the implications of these results.

5.1. Complexity of Rupture and Breaking of Young Faults

Although the faults involved in this rupture were not previously mapped, the seafloor fabric in this region is known to be a complex mixture of structures inherited from past geological epochs, and the majority of seismicity in the Wharton Basin has been inferred to be related to reactivation of the ocean fabric [*Delescluse et al.*, 2012]. *Delescluse et al.* [2008] suggest that reactivation is selective, with evidence that some structures have been abandoned.

Seismic reflection profiles acquired ~110 km north of the epicenter show a mixture of structures that include fracture zones, pull-apart basins, flower structures, and some faults that have dip-slip motion on strike-slip faults [*Carton et al.*, 2014]. Average fault spacing is ~10–20 km. These survey results include evidence for WNW striking structures to the west of the NNE trending fracture zone. The WNW striking mapped structures extend >7 km into oceanic mantle, are estimated to have a maximum depth of ~37 km below sea level, and appear to be dip slip [*Carton et al.*, 2014]. Surveys in the area of the northern NER also show a complex pattern of faults, including faults that were originally normal reactivated as strike slip with a component of compression [*Sager et al.*, 2013]. The diffuse pattern of aftershocks (Figure 2), albeit likely with location errors, suggest activation of many unmapped faults and not only those on which we model slip. (The band of aftershocks parallel to the Sunda trench, for example, may represent a process related to plate bending along the subduction zone

[*Masson*, 1991; *Ranero et al.*, 2005].) The majority of aftershocks with focal mechanisms in the Global Centroid Moment Tensor (GCMT) catalog are strike slip, but some are extensional/oblique.

Given the complexity in rakes and dips observed by the geophysical surveys, it is difficult to infer what rakes and dips we should expect on our faults. Our preferred model has north dipping thrust motion on Fault 1, thrust motion on a vertical Fault 2, and pure strike-slip motion on west dipping NNE faults (Figure 6). However, the many tradeoffs in our inversion mean that we do not necessarily believe these to be the physical geometry. Many other variations of rake and dip will also fit the data well, and the general conclusions of the paper are robust with alternate geometries. For example, we know that the NNE trending faults north of this rupture dip to the east, as imaged by *Carton et al.* [2014]. Either the dip of the fault changes along strike (which would not be unexpected, given that this originated as a fracture zone), or our estimated dip is incorrect. To test the sensitivity of our results, we therefore tested our model with an east dipping NNE fault. The change does not significantly impair the model fits (Figure 11). All we can say conclusively about the fault geometry is that vertical, pure strike-slip faults are unlikely, as this does not result in a good model fit to the data.

We should not be too surprised by complexity in this rupture. Although rare, oceanic lithosphere events have a history of being so; past oceanic earthquakes include examples of cross faulting (in the same event), rupture across different fault segments separated by large distances, reactivation of old structures with new senses of slip, and rupture of unmapped fault traces despite the existence of more prominent seafloor features:

1. As an example of cross faulting of oceanic lithosphere, the 18 June 2000 M_w 7.8 Wharton Basin earthquake possibly involved rupture of both N-S and E-W trending fault planes during the same event [*Robinson et al.*, 2001; *Abercrombie et al.*, 2003].
2. The 1998 M_w 8.1 Balleny Islands (Antarctic Plate) earthquake is an example of an event that ruptured faults that did not coincide with any known features on the ocean floor, ruptured at high angle to existing fracture zones, and may have had several subevents on different fault planes. Although debated, it may have jumped an unbroken barrier ≥70 km long [*Henry et al.*, 2000; *Hjörleifsdóttir et al.*, 2009].
3. The 1994 M_w 7.0 Romanche (mid-Atlantic Ridge) earthquake was also complex, may have involved jumping to another fault and had a rupture strike that was not parallel to lineations visible in gravity, to the trend of propagating rift trails or to predicted magnetic anomalies [*McGuire et al.*, 1996; *Abercrombie and Ekström*, 2001].
4. The 2004 M_w 8.1 Tasman Sea earthquake demonstrated the reactivation of old structures with a new mechanism, rupturing an old spreading ridge as a strike-slip rupture [*Robinson*, 2011].
5. Even on land, we know that it is not uncommon to generate large earthquakes on faults that were not previously mapped, even in the presence of well-mapped and important neighboring faults. Well-known examples include the 1999 M_w 7.1 Hector Mine [e.g., *Jachens et al.*, 2002] and the 2010 M_w 7.0 Haiti [*Calais et al.*, 2010] earthquakes.

An obvious reason for complexity in these types of events is that the inherited plate fabric from seafloor spreading is complex, and the inherited structures are often not optimally oriented for the present-day stress field, as with the NNE trending faults in this earthquake. In the case of the 2012 sequence, however, the number of distinct faults involved seems truly exceptional.

Also exceptional is the high level of slip on these many distinct faults. As a thought experiment, take a rate of 1 cm/yr on a single fault; the time needed to build up enough stress for the levels of slip we observe would be ~4000 years. With more faults involved, the recurrence time must be considerably longer than this. Hence, this might be a very rare sequence.

The NNE trending faults are old, deep, lithospheric fracture zones, and prominent features of the seafloor. It is generally assumed that fracture will follow the path of least resistance and rupture existing structures, even when they are not optimally oriented for the present-day stress field. It could, therefore, be seen as surprising that the younger, unmapped, WNW trending faults ruptured with more moment, and also perhaps surprising that it is these young faults that seem to have accommodated the deepest slip, rather than the old faults that are recognized to cut through the entire lithosphere. However, it may simply be the case that the WNW trending faults are more optimally oriented for the present-day stress field than the NNE trending faults.

The angle between the NNE and WNW trending faults in our optimized geometry is 80°. This is wider than the ~60° which is commonly observed between conjugate shear faults. One explanation for this is that the NNE trending faults were preexisting structures, the WNW trending faults perhaps also so (e.g., born along

slightly oblique initial Wharton spreading center crustal normal faults), and the wide angle is simply a result of the preexisting structures. Alternatively, that this angle is ~80° may reflect the fact that the driving stresses are deep.

The common 60° angle for conjugate faults is associated with failure under the linear Mohr-Coulomb failure criterion with Byerlee friction values (0.6–0.85). Such failure requires significant dilatancy; frictional sliding involves breaking microcracks and small asperities between the two surfaces, which requires some amount of volume change. Upper crustal faults experience relatively low confining pressure and can accommodate dilatancy. However, at the depths of estimated slip for this event we would expect high confining pressure, and negligible dilatancy; it would be difficult to deform rocks with any volume increase at such depth [*Brace et al.*, 1966; *Cherry et al.*, 1975; *Tapponnier and Brace*, 1976]. With no volume change, linear Mohr-Coulomb failure is no longer appropriate. Under these conditions, the failure envelope as plotted on a Mohr stress diagram flattens (e.g., by the Von Mises criterion [e.g., *van Der Pluijm and Marshak*, 2004]), implying predominantly grain boundary sliding rather than dilatant cracking as the main mechanism of brittle deformation and giving an angle of 90° between optimally oriented conjugate shear zones [*van Der Pluijm and Marshak*, 2004; *Eberhardt*, 2012]. As a consequence, our observed value of 80° may reflect the formation of these deep faults in an environment that requires a significant level of grain boundary sliding.

If we then assume, for the sake of argument, that the WNW trending faults formed due to the present-day stress field we can estimate that the σ_1 principal stress direction should be ~30–40° from the orientation of these faults. Our results imply that these faults have an orientation of ~292°, placing estimates for the orientation of σ_1 at ~322–332°.

The above reasoning results in a ~50–60° angle between σ_1 and the NNE trending fracture zones. Depending on what is the optimal orientation between faults and the σ_1 direction for this case, as discussed above, this represents a ~10–20° divergence from the optimal orientation. Although in these assumptions the WNW faults are better oriented for the present-day stress field, a 20° divergence is not so large that the existing NNE trending structures are not reactivated [*Sibson*, 1985, 1990; *Masson*, 1991; *Henza et al.*, 2010].

The present-day stress field for the Wharton Basin has not been well-resolved by other methods, but we do know that the Australian plate is moving toward the Indian Plate at ~316° [*DeMets et al.*, 2010; *Duputel et al.*, 2012]. If we assume that this also reflects the orientation of σ_1, our estimate (based on the very simple assumptions described above) would be a little high. This could confirm the existence of the WNW trending faults as also being preexisting structures that are not optimally aligned with the present-day stress field. Alternatively, the assumption that the rate of plate convergence reflects the orientation of σ_1 is oversimplified.

5.2. Deep Rupture of the Younger Faults

As with the complexity of rupture, we should not be too surprised that the event ruptured into the mantle, below the ~12 km deep Moho:

1. Geophysical surveys in the Wharton Basin have shown evidence of faulting that extends beneath the oceanic Moho [e.g., *Bull and Scrutton*, 1990; *Carton et al.*, 2014].
2. Other oceanic earthquakes have also been deep. For example, the 1989 M_s 8.2 Macquerie Ridge earthquake (deepest slip 12–16 km) [*Anderson and Zhang*, 1991], the 1998 M_s 8.1 Antarctic Plate (centroid depths 16–26 km) [*Henry et al.*, 2000], the 2003 M_s 7.6 Mid-Indian Ocean (large slip ≥20 km depths) [*Antolik et al.*, 2006]. and various events on the Romanche transform (centroid depths of 7–20 km) [*Abercrombie and Ekström*, 2001] have been estimated to rupture below the Moho to various extents.
3. Unlike continental earthquakes, slip in oceanic earthquakes is expected to rupture into the mantle based on the composition of the oceanic mantle and its thermal profile. The brittle-ductile transition may be around 50 km depth. Experimental data indicate that olivine-rich materials will transition from velocity weakening to velocity strengthening at ~600°C when subjected to the geological conditions expected at the base of the oceanic lithosphere [*Boettcher et al.*, 2007] (with this geotherm usually located at depths of 20–40 km in oceanic lithosphere).
4. The 600°C geotherm has also been estimated as an approximate limit for seismic rupture by analysis of oceanic transform fault earthquakes using broadband seismic data [*Abercrombie and Ekström*, 2001].

We might, however, be surprised that the rupture extended deeper than the estimated depth of the 600°C geotherm. At the location of our faults, the 600°C geotherm is estimated to be at ~30 km depth based on a diffusion model [*Stein and Stein*, 1992] and plate ages from *Müller et al.* [1997]. The geotherm is estimated

to be at a depth of ~35 km in the vicinity of the NER to the west, and shallows to ≤30 km to the east of our faults. (The plate gets younger from west to east, and the fracture zones represent jumps in plate age and therefore thickness.) The 1125°C geotherm depth at the location of the faults is estimated to be ~70–75 km. To compare with these numbers, slip on Faults 1 and 2 decays fairly smoothly from the surface to depths of at least 60 km (Figure 6). The largest slip estimates are shallower than 30 km, but there is still ≥8 m slip estimated between 30 and 60 km.

The frictional properties of the oceanic lithosphere are poorly known. However, it is generally agreed that frictional failure becomes increasingly unlikely at temperatures ≥ 600 ± 100°C [*Chen and Molnar*, 1983; *Kirby and Kronenberg*, 1987; *Abercrombie and Ekström*, 2001; *McGuire and Beroza*, 2012] and under the high-pressure conditions at the depths associated with these temperatures [*McGuire and Beroza*, 2012]. The fact that the cross faults are at a wide angle may, as discussed in section 5.1, also reflect the high-pressure, low-dilatancy environment, implying failure is toward the more ductile side of the spectrum. The significant depth of the April 2012 ruptures, therefore, suggests either that an alternative mechanism for rupture may be necessary, or that the geotherm and brittle-ductile transition are considerably deeper than previously thought.

In the case of an alternative mechanism, it is possible that deep slip was generated by a process of thermal weakening [*Kanamori et al.*, 1998; *Di Toro et al.*, 2006; *Keleman and Hirth*, 2007; *Brown and Fialko*, 2012], as suggested by *McGuire and Beroza* [2012]. By this process, heat generated in a fine-grained shear zone generates a thermal runaway feedback system, resulting in localized zones of viscous failure [e.g., *Keleman and Hirth*, 2007]. When the rupture is particularly deep (i.e., high pressure), and the slip is large enough, the fault will melt [*Kanamori et al.*, 1998; *McGuire and Beroza*, 2012].

Supporting this idea, we note that 72% of the aftershocks from this earthquake were crustal (Figure 2). Previous authors have raised the question of whether aftershocks for oceanic earthquakes behave like their continental counterparts (i.e., cluster outside the areas of largest coseismic rupture), or whether they are somehow different [*Antolik et al.*, 2006]. In the case of this earthquake, the relative absence of deep aftershocks may support the idea that while slip can propagate into the deeper fault in certain conditions, this part of the fault is velocity strengthening at plate rate, and unable to initiate seismic slip.

However, it is also possible that no unusual rupture mechanism is required and that the brittle-ductile transition is simply deeper than (or, indeed, at) the bottom of our estimated rupture patch. The brittle-ductile transition can be affected by factors such as the stress regime and strain rate and may be as deep as 750°C in the Indian Ocean region [*Weins and Stein*, 1984]. Furthermore, the oceanic mantle lithosphere thickens away with distance from the ridge axis in a simple, thermally driven cooling process and becomes older, colder, and stronger between fracture zones; it would not be too surprising that the geotherm depths are underestimated.

The old NNE trending faults were born as translithospheric, while the WNW trending faults are assumed to have been born as crustal faults that have propagated into the lithospheric mantle. It could also, therefore, be seen as puzzling that it was the WNW trending faults that have the deep slip, not the NNE trending faults. This could be connected to the thermal weakening process. Alternatively, this could be representative of the fact that it is difficult to break the old, cold, strong lithosphere between fracture zones, and therefore, when these faults do rupture they do so spectacularly.

5.3. Rupture of Faults Along the Ninety East Ridge

The late arrivals in the hrGPS waveforms are best fit by rupture along a structure that lies along the trace of the NER. It is possible that a perpendicular structure (Fault 6a in Figure 2) also ruptured, but these faults are far from our networks, and we do not have the resolution to tell. Results from backprojection and previous inversions have also been ambiguous, for example, *Yue et al.* [2012] invert for slip on a WNW trending geometry, but say it could be either this or a NNE trending structure.

The modern consensus is that the NER was created by hot spot volcanism that emplaced a ridge on the northward drifting Indian plate from Late Cretaceous to early Cenozoic times [*Krishna et al.*, 2012]. The nature of deformation along this ridge is poorly understood, but it seems to represent a mechanical boundary between the different styles of deformation in the Central Indian Basin and the Wharton Basin [*Sager et al.*, 2013]. For this ridge to serve as this boundary there would have to be a complex system of faults; seismic reflection surveys have shown that the fault pattern is highly variable along its length [*Tinnon et al.*, 1995; *Delescluse and Chamot-Rooke*, 2007; *Sager et al.*, 2013; *Andrade and Rajendran*, 2014]. The NER is cut along its length by E-W

lineations and horst-and-graben features, and some sections do not show evidence of strike-slip faults with N-S orientations [*Sager et al.*, 2013; *Andrade and Rajendran*, 2014]. Our interpretation of slip on this feature is therefore likely to be highly simplified and may represent the cumulative rupture of a number of small faults. Indeed, our "optimized" fault does not seem to line up well with the NNE trending aftershocks (Figure 2), possibly because we are modeling slip on some combination of smaller faults.

5.4. Large Variations in Stress Drop

The large magnitude of the event was due to a combination of the large number of faults involved, and the fact that it ruptured high-rigidity mantle material. Whether it was also due to a high stress drop, however, is less clear. Past studies have hypothesized that high stress drops may be expected for ruptures on oceanic transform faults [e.g., *Anderson and Zhang*, 1991; *Robinson et al.*, 2001; *Antolik et al.*, 2006; *Robinson*, 2011] and, indeed, previous publications have suggested high stress drop for this event [e.g., *Meng et al.*, 2012]. In a global survey *Choy and Boatwright* [1995] concluded that oceanic strike-slip events have the highest apparent stress of all the events they studied. *Antolik et al.* [2006] discuss observations that large earthquakes occurring in oceanic lithosphere have often exhibited low aftershock to main shock energy ratios, which could suggest that complete stress drop is common for these types of events.

Our estimate for total event stress drop of ~14–17 MPa suggests a value for this event that is on the high side but not extremely high. To reach this conclusion, we recalculated stress drops for a collection of other strike-slip events, using the same stress drop calculations (section 4) and published slip distributions. Unlike comparisons where scientists have had to (often rather arbitrarily) decide on the rupture area to use in analytical calculations of stress drop, this technique allows for a more robust comparison. Examples include 24 MPa (Landers M_w 7.3 1992, [*Fialko*, 2004]), 13 MPa (Hector Mine M_w 7.1 1999 [*Simons et al.*, 2002]), and 8 MPa (El Mayor M_w 7.2 2010, [*Fialko et al.*, 2010]). We also recalculated the stress drop for this event using the slip distribution of *Wei et al.* [2013] and obtained a slightly lower but similar value to ours, at 12 MPa. We make these comparisons with the caveat that stress drop in finite-fault inversions is poorly constrained, has an inverse correlation with smoothing weight, and is often a function of the level of analysis and volume of data available. We also note that we used a shear modulus of 30 GPa for all events, to enable comparison, but the rigidity of the oceanic lithosphere is likely to be considerably higher.

This said, our Fault 1 (the primary WNW trending fault) has a very high stress drop of ~25 MPa, considerably higher than the other faults and high relative to other events. Fault 2 also had higher stress drop than the other faults. In addition to exhibiting the highest levels of slip, these faults also accommodated the deepest slip. These results differ from those of *Wei et al.* [2013], who placed their high stress drops on the NNE trending fault. (Their model uses regional and telseismic waveform data, and a different fault geometry.)

If a fault is more mature, it may be less segmented. With less segmentation, rupture can propagate with less obstacles and generate more slip. With a more segmented fault, the rupture propagates across velocity-strengthening barriers or geometrical obstacles that impede slip; the overall coseismic slip is decreased for the same rupture distance, leading to a lower stress drop. Since they are such prominent features of the seafloor, it is tempting to think of the NNE trending fracture zones as well-established faults. However, these are actually reactivated structural boundaries between older and younger crust (rather than well-established faults), and thus may have many steps and barriers. Thus, we would not necessarily expect high stress drop on these structures, as observed. Furthermore, it is common that fracture zones are lubricated with serpentinite [e.g., *Francis*, 1981], which could make them weaker and cause rupture with less high-frequency seismic radiation (as with the shallow areas of subduction megathrusts) [*Dengo and Logan*, 1981; *Reinen et al.*, 1991; *Katayama et al.*, 2013].

On the younger faults, however, we do observe high stress drop. One explanation for this is to invoke—as discussed in section 5.2—an alternative failure mechanism such as thermal weakening, which could produce high stress drop through strong weakening [e.g., *Fialko and Khazan*, 2005; *Di Toro et al.*, 2006; *Beeler et al.*, 2008; *Di Toro et al.*, 2011]. Alternatively, the high stress drops (and deep slip) on the young faults are simply because they are strong and difficult to break.

5.5. Long Event Duration

Some studies have suggested that the event involved supershear rupture on some segments [*Wang et al.*, 2012], while others have suggested relatively slow rupture speeds, given the location of the event below the oceanic Moho [*Meng et al.*, 2012]. Having a better knowledge of rupture velocity would lead to a better

understanding of the physics and friction parameters of this unusual earthquake. Unfortunately, however, we cannot provide additional constraints on the rupture velocity. The rupture velocity trades off with parameters such as hypocenter location, so an exploration of different velocities does not yield conclusive results. We do, however, show that models produced using a rupture velocity of 2.0 km/s (as suggested in previous studies such as *Yue et al.* [2012]; *Wei et al.* [2013]) will fit the data well. The data also confirm, unsurprisingly, the long duration of the event, with rupture of the final fault segment ending at ~180 s. Long durations are common for oceanic earthquakes [*Antolik et al.*, 2006; *Perez-Campos et al.*, 2003; *Ekstrom et al.*, 1992], perhaps in part due to relatively slow rupture speeds but also simply as a result of the long stretches of fault that rupture.

6. Conclusions

In our introduction we posed a number of questions. To summarize our findings with respect to these questions we found that

1. The majority of moment release for this event occurred on WNW trending faults, rather than on the more prominent NNE trending faults that are evident in the seafloor fabric. Our results indicate the value in including, for the first time, high-rate GPS observations from the nearby region in analysis of this complicated event; if we invert only the teleseismic data there is remaining ambiguity in the relative importance of the NNE versus WNW trending faults, but the GPS data show a strong preference for the WNW trending faults.
2. Many different fault sections ruptured in this event. These include a fault ~400 km to the west of the hypocenter, in the location of the Ninety East Ridge, as evidenced by late-arriving waveforms in the high-rate GPS data.
3. The GPS data also provide—particularly through examination of the nodal plane of the static displacements—new constraints on the strike of the WNW trending faults. The WNW and NNE trending faults are at a wide angle. This may be the simple result of either or both sets being preexisting structures left over from the Eocene spreading center. Alternatively, this angle may be a result of their formation at depth, optimal within the present-day stress field and in a high-pressure, low-dilatancy environment.
4. The slip was deep and extended into the oceanic mantle. While our resolution of the exact depth extent remains relatively poor, we reliably see slip down to at least 60 km.
5. The event had such a large magnitude because so many segments were involved and because some faults experienced very large slip in high-rigidity material. The young, WNW trending faults experienced the largest slip and high stress drops.

The 2012 Wharton Basin earthquake sequence illuminates a deformation zone that may represent the formation of a new, localized, plate boundary between the Indian and Australian Plates. That so many faults ruptured in a cascade during this event sequence is an indication that no kinematically acceptable single large fault yet exists to relieve the stress imparted by the relative plate motion; many more events like this would be needed to create a distinct plate boundary, and it will be a long time before scientists know the extent to which the boundary remains diffuse by nature.

The oceanic lithosphere between the fracture zones is older, colder, stronger, and while the crust is pervaded with faults and preexisting structures the mantle should not be. Hence, the strongest faults should be any that are transverse to the fracture zones. That it is difficult to break the mantle in between the fracture zones may be the reason that there is not yet a throughgoing plate boundary between the India and Australia Plates, and why recurrence times are very long; the fracture zones are not optimally oriented for the present-day stress field, but breaking new faults here is not easy. A combination of this strength and a deep brittle-ductile transition (or the triggering of an alternative rupture mechanism such as thermal weakening) may explain the fact that the highest and deepest slip, and highest stress drop, was observed on the WNW trending faults.

References

Abercrombie, R., M. Antolik, and G. Ekström (2003), The June 2000 M_w 7.9 earthquakes south of Sumatra: Deformation in the India-Australia Plate, *J. Geophys. Res.*, *108*(B1), 2018, doi:10.1029/2001JB000674.

Abercrombie, R. E., and G. Ekström (2001), Earthquake slip on oceanic transform faults, *Nature*, *410*(6824), 74–77.

Akaike, H. (1980), Likelihood and the Bayes procedure, in *Bayesian Statistics*, edited by J. M. Bernardo et al., pp. 143–166, Univ. Press, Valencia, Spain.

Amante, C., and B. W. Eakins (2009), ETOPO1 1 arc-minute global relief model: Procedures, data sources and analysis, *Tech. Rep. NOAA NESDIS NGDC-24*, Natl. Geophys. Data Cent., NOAA, Boulder, Colo., doi:10.7289/V5C8276M.

Anderson, H. J., and J. Zhang (1991), Long-period seismic radiation from the May 23, 1989, Macquire Ridge earthquake: Evidence for coseismic slip in the mantle?, *J. Geophys. Res.*, *96*(B12), 19,853–19,863.

Andrade, V., and K. Rajendran (2014), The April 2012 Indian Ocean earthquakes: Seismotectonic context and implications for their mechanisms, *Tectonophysics*, *617*, 126–139, doi:10.1016/j.tecto.2014.01.024.

Antolik, M., R. E. Abercrombie, J. Pan, and G. Ekström (2006), Rupture characteristics of the 2003 M_W 7.6 mid-Indian Ocean earthquake: Implications for seismic properties of young oceanic lithosphere, *J. Geophys. Res.*, *111*, B04302, doi:10.1029/2005JB003785.

Beeler, N. M., T. E. Tullis, and D. L. Goldsby (2008), Constitutive relationships and physical basis of fault strength due to flash heating, *J. Geophys. Res.*, *113*, B01401, doi:10.1029/2007JB004988.

Bertiger, W., S. D. Desai, B. Haines, N. Harvey, A. W. Moore, S. Owen, and J. P. Weiss (2010), Single receiver phase ambiguity resolution with GPS data, *J. Geod.*, *84*, 327–337, doi:10.1007/s00190-010-0371-9.

Bird, P. (2003), An updated digital model of plate boundaries, *Geochem. Geophys. Geosyst.*, *4*(3), 1027, doi:10.1029/2001GC000252.

Blewitt, G. (1989), Carrier phase ambiguity resolution for the Global Positioning System applied to geodetic baselines up to 2000 km, *J. Geophys. Res.*, *94*(B8), 10,187–10,203.

Boettcher, M. S., G. Hirth, and B. Evans (2007), Olivine friction at the base of oceanic seismogenic zones, *J. Geophys. Res.*, *112*, B01205, doi:10.1029/2006JB004301.

Brace, W. F., B. W. Paulding, and C. Scholz (1966), Dilatancy in the fracture of crystalline rocks, *J. Geophys. Res.*, *71*(16), 3939–3953.

Bradley, A. M. (2014), Software for efficient static dislocation-traction calculations in fault simulators, *Seismol. Res. Lett.*, *86*(1), 1358–1365.

Brown, K., and Y. Fialko (2012), 'Melt welt'mechanism of extreme weakening of gabbro at seismic slip rates, *Nature*, *488*, 638–641, doi:10.1038/nature11370.

Bull, J. M., and R. A. Scrutton (1990), Fault reactivation in the central Indian Ocean and the rheology of oceanic lithosphere, *Nature*, *344*, 855–858.

Calais, E., A. Freed, G. Mattioli, F. Amelung, S. Jónsson, P. Jansma, S.-H. Hong, T. Dixon, C. Prépetit, and R. Momplaisir (2010), Transpressional rupture of an unmapped fault during the 2010 Haiti earthquake, *Nat. Geosci.*, *3*, 794–799, doi:10.1038/NGEO992.

Carton, H., S. Singh, N. Hananto, J. Martin, Y. Djajadihardja, D. Franke Udrekh, and C. Gaedicke (2014), Deep seismic reflection images of the Wharton Basin oceanic crust and uppermost mantle offshore Northern Sumatra: Relation with active and past deformation, *J. Geophys. Res. Solid Earth*, *119*, 32–51, doi:10.1002/2013JB010291.

Chamot-Rooke, N., F. Jestin, B. de Voogd, and P. W. Group (1993), Intraplate shortening in the central Indian Ocean determined from a 2100-km-long north-south deep seismic reflection profile, *Geology*, *21*, 1043–1046.

Chen, W.-P., and P. Molnar (1983), Focal depths of intercontinental and intraplate earthquakes and their implications for the thermal and mechanical properties of the lithosphere, *J. Geophys. Res.*, *88*(B5), 4183–4214.

Cherry, J. T., R. N. Schock, and J. Sweet (1975), A theoretical model of the dilatant behavior of a brittle rock, *Pure Appl. Geophys.*, *113*, 183–196.

Choy, G. L., and J. L. Boatwright (1995), Global patterns of radiated seismic energy and apparent stress, *J. Geophys. Res.*, *100*(B9), 18,205–18,228.

Cloetingh, S., and R. Wortel (1986), Stress in the Indo-Australian Plate, *Tectonophysics*, *132*, 49–67, doi:10.1016/0040-1951(86)90024-7.

Delescluse, M., and N. Chamot-Rooke (2007), Instantaneous deformation and kinematics of the India-Australia Plate, *Geophys. J. Int.*, *162*(2), 818–842, doi:10.1111/j.1365-246X.2006.03181.x.

Delescluse, M., and N. Chamot-Rooke (2008), Serpentinization pulse in the actively deforming Central Indian Basin, *Earth Planet. Sci. Lett.*, *276*, 140–151, doi:10.1016/j.epsl.2008.09.017.

Delescluse, M., L. G. J. Montési, and N. Chamot-Rooke (2008), Fault reactivation and selective abandonment in the oceanic lithosphere, *Geophys. Res. Lett.*, *35*, L16312, doi:10.1029/2008GL035066.

Delescluse, M., N. Chamot-Rooke, R. Cattin, L. Fleitout, O. Trubienko, and C. Vigny (2012), April 2012 intra-oceanic seismicity off Sumatra boosted by the Banda-Aceh megathrust, *Nature*, *490*, 240–244, doi:10.1038/nature11520.

DeMets, C., R. G. Gordon, and D. F. Argus (2010), Geologically current plate motions, *Geophys. J. Int.*, *181*, 1–80, doi:10.1111/j.1365-246X.2009.04491.x.

Dengo, C. A., and J. M. Logan (1981), Implications of the mechanical and frictional behavior of serpentinite to seismogenic faulting, *J. Geophys. Res.*, *86*(B11), 10,771–10,782, doi:10.1029/JB086iB11p10771.

DePlus, C. (2001), Indian Ocean actively deforms, *Science*, *292*, 1850–1851.

DePlus, C., et al. (1998), Direct evidence of active deformation in the eastern Indian oceanic plate, *Geology*, *26*(2), 131–134.

Di Toro, G., T. Hirose, S. Nielsen, G. Pennacchioni, and T. Shimamoto (2006), Natural and experimental evidence of melt lubrication of faults during earthquakes, *Science*, *311*, 647–649, doi:10.1126/science.1121012.

Di Toro, G., R. Han, T. Hirose, N. de Paola, S. Nielsen, K. Mizoguchi, F. Ferri, M. Cocco, and T. Shimamoto (2011), Fault lubrication during earthquakes, *Nature*, *471*, 494–498, doi:10.1038/nature09838.

Duputel, Z., H. Kanamori, V. C. Tsai, L. Rivera, L. Meng, J.-P. Ampuero, and J. M. Stock (2012), The 2012 Sumatra great earthquake sequence, *Earth. Planet. Sci. Lett.*, *351–352*, 247–257.

Dziewonski, A. M., and D. L. Anderson (1981), Preliminary reference Earth model, *Phys. Earth Planet. Inter.*, *25*(4), 297–356, doi:10.1016/00319201(81)90046-7.

Eberhardt, E. (2012), The Hoek-Brown failure criterion, *Rock Mech. Rock Eng.*, *45*, 981–988, doi:10.1007/s00603-012-0276-4.

Ekström, G., M. Nettles, and A. M. Dziewonski (2012), The global CMT project 2004–2010: Centroid-moment tensors for 13,017 earthquakes, *Phys. Earth Planet. Inter.*, *200–201*, 1–9, doi:10.1016/j.pepi.2012.04.002.

Elosegui, P., J. L. Davis, J. M. Johansson, and I. I. Shapiro (1996), Detection of transient motions with the global positioning system, *J. Geophys. Res.*, *101*(B5), 11,249–11,261.

Fialko, Y. (2004), Probing the mechanical properties of seismically active crust with space geodesy: Study of the coseismic deformation due to the 1992 M_W 7.3 Landers (southern California) earthquake, *J. Geophys. Res.*, *109*, B03307, doi:10.1029/2003JB002756.

Fialko, Y., and Y. Khazan (2005), Fusion by earthquake fault friction: Stick or slip?, *J. Geophys. Res.*, *110*, B12407, doi:10.1029/2005JB003869.

Fialko, Y., A. Gonzales, J. J. Gonzales-Garcia, S. Barbot, S. Leprince, D. T. Sandwell, and D. C. Agnew (2010), Static rupture model of the 2010 M7.2 El Mayor-Cucapah earthquake from ALOS, ENVISAT, SPOT and GPS data, Abstract T53B–2125 presented at 2010 Fall Meeting, AGU, San Francisco, Calif., 13–17 Dec.

Francis, T. J. G. (1981), Serpentinization faults and their role in the tectonics of slow spreading ridges, *J. Geophys. Res.*, *86*(B12), 11,616–11,622, doi:10.1029/JB086iB12p11616.

Gordon, G. G. (1998), The plate tectonic approximation: Plate nonrigidity, diffuse plate boundaries, and global plate reconstructions, *Annu. Rev. Earth Planet. Sci.*, *26*, 615–642.

Harris, R. A., and P. Segall (1987), Detection of a locked zone at depth on the Parkfield, California, segment of the San Andreas fault, *J. Geophys. Res.*, *92*(B8), 7945–7962.

Hartzell, S. H., and T. H. Heaton (1983), Inversion of strong ground motion and teleseismic waveform data for the fault rupture history of the 1979 Imperial Valley, California, earthquake, *Bull. Seismol. Soc. Am.*, *73*(6), 1553–1583.

Henry, C., S. Das, and J. H. Woodhouse (2000), The great March 25, 1998, Antarctic Plate earthquake: Moment tensor and rupture history, *J. Geophys. Res.*, *105*(B7), 16,097–16,118.

Henza, A. A., M. O. Withjack, and R. W. Schlische (2010), Normal-fault development during two phases of non-coaxial extension: An experimental study, *J. Struct. Geol.*, *32*, 1656–1667, doi:10.1016/j.jsg.2009.07.007.

Hjörleifsdóttir, V., H. Kanamori, and J. Tromp (2009), Modeling 3-D wave propagation and finite slip for the 1998 Balleny Islands earthquake, *J. Geophys. Res.*, *114*, B03301, doi:10.1029/2008JB005975.

Ishii, M., E. Kiser, and E. L. Geist (2013), M_W 8.6 Sumatran earthquake of 11 April 2012: Rare seaward expression of oblique subduction, *Geology*, *41*(3), 319–322, doi:10.1130/G33783.1.

Jachens, R. C., V. E. Langenheim, and J. C. Matti (2002), Relationship of the 1999 Hector Mine and 1992 Landers fault ruptures to offsets on Neogene faults and distribution of late Cenozoic basins in the eastern California shear zone, *Bull. Seismol. Soc. Am.*, *92*(4), 1592–1605.

Jacob, J., J. Dyment, and V. Yatheesh (2014), Revisiting the structure, age and evolution of the Wharton Basin to better understand subduction under Indonesia, *J. Geophys. Res. Solid Earth*, *119*, 169–190, doi:10.1002/2013JB010285.

Kanamori, H., and D. J. Anderson (1975), Theoretical basis of some empirical relations in seismology, *Bull. Seismol. Soc. Am.*, *65*(5), 1073–1095.

Kanamori, H., D. J. Anderson, and T. H. Heaton (1998), Frictional melting during the rupture of the 1994 Bolivian Earthquake, *Science*, *279*, 839–842.

Katayama, I., M. Iwata, K. Okazaki, and K. Hirauchi (2013), Slow earthquakes associated with fault healing on a serpentinized plate interface, *Sci. Rep.*, *3*, 1784, doi:10.1038/srep01784.

Keleman, P. B., and G. Hirth (2007), A periodic shear-heating mechanism for intermediate-depth earthquakes in the mantle, *Nature*, *446*, 787–790, doi:10.1038/nature05717.

Kikuchi, M., H. Kanamori, and K. Satake (1993), Source complexity of the 1988 Armenian earthquake: Evidence for a slow after-slip event, *J. Geophys. Res.*, *98*(B9), 15,797–15,808.

Kirby, S. H., and A. K. Kronenberg (1987), Rheology of the lithosphere: Selected topics, *Rev. Geophys.*, *25*(6), 1219–1244.

Krishna, K. S., H. Abraham, W. W. Sager, M. S. Pringle, F. Frey, D. G. Rao, and O. V. Levchenko (2012), Tectonics of the Ninetyeast Ridge derived from spreading records in adjacent oceanic basins and age constraints of the ridge, *J. Geophys. Res.*, *117*, B04101, doi:10.1029/2011JB008805.

Lawson, C. L., and R. J. Hanson (1974), *Solving Least Squares Problems*, SIAM, N. J.

Masson, D. G. (1991), Fault patterns at outer trench walls, *Mar. Geophys. Res.*, *13*, 209–225.

McAdoo, D. C., and D. T. Sandwell (1985), Folding of oceanic lithosphere, *J. Geophys. Res.*, *90*(B10), 8563–8569.

McGuire, J. J., and G. C. Beroza (2012), A rogue earthquake off Sumatra, *Science*, *336*, 1118–1119.

McGuire, J. J., P. F. Ihmle, and T. H. Jordan (1996), Time-domain observations of a slow precursor to the 1994 romanche transform earthquake, *Science*, *274*, 82–85.

Meng, L., J.-P. Ampuero, J. Stock, Z. Duputel, Y. Luo, and V. C. Tsai (2012), Earthquake in a maze: Compressional rupture branching during the 2012 M_W 8.6 Sumatra earthquake, *Science*, *336*, 1118–1119.

Minster, J. B., and T. H. Jordan (1978), Present-day plate motions, *J. Geophys. Res.*, *83*(B11), 5331–5354.

Müller, R. D., W. R. Roest, J.-Y. Royer, L. M. Gahagan, and J. G. Sclater (1997), Digital isochrons of the world's ocean floor, *J. Geophys. Res.*, *102*(B2), 3211–3214.

Noda, H., N. Lapusta, and H. Kanamori (2013), Comparison of average stress drop measures for ruptures with heterogeneous stress change and implications for earthquake physics, *Geophys. J. Int.*, *193*, 1691–1712, doi:10.1093/gji/ggt074.

Okada, Y. (1992), Internal deformation due to shear and tensile faults in a half-space, *Bull. Seismol. Soc. Am.*, *82*(2), 1018–1040.

Olsen, A. H., and R. J. Apsel (1982), Finite faults and inverse theory with applications to the 1979 Imperial Valley earthquake, *Bull. Seismol. Soc. Am.*, *72*, 1969–2001.

Pasyanos, M. E., T. G. Masters, G. Laske, and Z. Ma (2014), Litho1.0: An updated crust and lithospheric model of the Earth, *J. Geophys. Res. Solid Earth*, *119*, 2153–2173, doi:10.1002/2013JB010626.

Petroy, D. E., and D. A. Wiens (1989), Historical seismicity and implications for diffuse plate convergence in the northeast Indian Ocean, *J. Geophys. Res.*, *94*(B9), 12,301–12,319.

Ranero, C. R., A. Villaseñor, J. P. Morgan, and W. Weinrebe (2005), Relationship between bend-faulting at trenches and intermediate-depth seismicity, *Geochem. Geophys. Geosyst.*, *6*, Q12002, doi:10.1029/2005GC000997.

Reinen, L. A., J. D. Weeks, and T. E. Tullis (1991), The frictional behavior of serpentinite: Implications for aseismic creep on shallow crustal faults, *Geophys. Res. Lett.*, *18*(10), 1921–1924, doi:10.1029/91GL02367.

Robinson, D. P. (2011), A rare great earthquake on an oceanic fossil fracture zone, *Geophys. J. Int.*, *186*(3), 1121–1134, doi:10.1111/j.1365-246X.2011.05092.x.

Robinson, D. P., C. Henry, S. Das, and J. H. Woodhouse (2001), Simultaneous rupture along two conjugate planes of the Wharton Basin earthquake, *Science*, *292*, 1145–1148.

Royer, J.-Y., and R. G. Gordon (1997), The motion and boundary between the Capricorn and Australian plates, *Science*, *277*, 1268–1274.

Sager, W. W., J. M. Bull, and K. S. Krishna (2013), Active faulting on the Ninetyeast Ridge and its relation to deformation of the Indo-Australian Plate, *J. Geophys. Res. Solid Earth*, *118*, 4648–4668, doi:10.1002/jgrb.50319.

Satriano, C., E. Kiraly, P. Bernard, and J.-P. Vilotte (2012), The 2012 M_W 8.6 Sumatra earthquake: Evidence of westward sequential seismic ruptures associated to the reactivation of a N-S ocean fabric, *Geophys. Res. Lett.*, *39*, L15302, doi:10.1029/2012GL052387.

Sekiguchi, H., K. Irikura, and T. Iwata (2000), Fault geometry at the rupture termination of the 1995 Hyogo-ken Nanbu earthquake, *Bull. Seismol. Soc. Am.*, *90*(1), 117–133.

Sibson, R. H. (1985), A note of fault reactivation, *J. Struct. Geol.*, *7*(6), 751–754.

Sibson, R. H. (1990), Rupture nucleation on unfavorably oriented faults, *Bull. Seismol. Soc. Am.*, *80*, 1580–1604.

Simons, M., Y. Fialko, and L. Rivera (2002), Coseismic deformation from the 1999 M_W 7.1 Hector Mine, California, earthquake as inferred from InSAR and GPS observations, *Bull. Seismol. Soc. Am.*, *92*(4), 1390–1402.

Singh, S. C., H. Carton, A. S. Chauhan, S. Androvandi, A. Davaille, J. Dyment, M. Cannat, and N. D. Hananto (2011), Extremely thin crust in the Indian Ocean possibly resulting from plume-ridge interaction, *Geophys. J. Int.*, *184*, 29–42, doi:10.1111/j.1365-246X.2010.04823.x.

Stein, C. A., and S. Stein (1992), A model for the global variation in oceanic depth and heat flow with lithospheric age, *Nature*, *359*, 123–129.

Stein, S., and E. A. Okal (1978), Seismicity and tectonics of the Ninetyeast Ridge area: Evidence for internal deformation of the Indian Plate, *J. Geophys. Res.*, *83*(B5), 2233–2245.

Subrahmanyam, C., R. Gireesh, S. Chand, K. A. K. Raju, and D. G. Rao (2008), Geophysical characteristics of the Ninetyeast Ridge — Andaman Island arc/trench convergent zone, *Earth Planet. Sci. Lett., 266*(1–2), 29–45.

Tapponnier, P., and W. F. Brace (1976), Development of stress-induced micro cracks in Westerly granite, *Int. J. Rock Mech. Min. Sci., 13*, 103–112.

Tinnon, M. J., W. E. Holt, and A. J. Haines (1995), Velocity gradients in the northern Indian Ocean inferred from earthquake moment tensors and relative plate motions, *J. Geophys. Res., 100*(B12), 24,315–24,329.

van Der Pluijm, B. A., and S. Marshak (2004), *Earth Structure*, 2nd ed., W. W. Norton and Co., New York.

Wang, D., J. Mori, and T. Uchide (2012), Supershear rupture on multiple faults for the M_w 8.6 off Northern Sumatra, Indonesia earthquake of April 11, 2012, *Geophys. Res. Lett., 39*, L21307, doi:10.1029/2012GL053622.

Wei, S., D. Helmberger, and J.-P. Avouac (2013), Modeling the 2012 Wharton basin earthquakes off-Sumatra: Complete lithospheric failure, *J. Geophys. Res. Solid Earth, 118*, 3592–3609, doi:10.1002/jgrb.50267.

Weins, D. A., and S. Stein (1984), Intraplate seismicity and stresses in young oceanic lithosphere, *J. Geophys. Res., 89*(B13), 11,442–11,464.

Wiens, D. A., et al. (1985), A diffuse plate boundary model for Indian Ocean tectonics, *Geophys. Res. Lett., 12*(7), 429–432.

Yadev, R. K., B. Kundu, K. Gahalaut, J. Catherine, V. K. Gahalaut, A. Ambikapthy, and M. S. Naidu (2013), Coseismic offsets due to the 11 April 2012 Indian Ocean earthquakes (M_w 8.6 and 8.2) derived from GPS measurements, *Geophys. Res. Lett., 40*, 3389–3393, doi:10.1002/grl.50601.

Yue, H., and T. Lay (2011), Inversion of high-rate (1 sps) GPS data for rupture process of the 11 March 2011 Tohoku earthquake (M_w 9.1), *Geophys. Res. Lett., 38*, L00G09, doi:10.1029/2011GL048700.

Yue, H., T. Lay, and K. D. Koper (2012), En échelon and orthogonal fault ruptures of the 11 April 2012 great intraplate earthquakes, *Nature, 490*, 245–249, doi:10.1038/nature11492.

Yue, H., T. Lay, S. Y. Schwartz, L. Rivera, M. Protti, T. H. Dixon, S. Owen, and A. V. Newman (2013), The 5 September 2012 Nicoya, Costa Rica M_w 7.6 earthquake rupture process from joint inversion of high-rate GPS, strong-motion, and teleseismic P wave data and its relationship to adjacent plate boundary interface properties, *J. Geophys. Res. Solid Earth, 118*, 5453–5466, doi:10.1002/jgrb.50379.

Zumberge, J. F., M. B. Heflin, D. C. Jefferson, M. M. Watkins, and F. H. Webb (1997), Precise point positioning for the efficient and robust analysis of GPS data from large networks, *J. Geophys. Res., 102*, 5005–5018.